Chemical Science

EDGE ARTICLE

View Article Online
View Journal | View Issue

Cite this: *Chem. Sci.*, 2016, **7**, 1156

Supramolecular aggregates of single-molecule magnets: exchange-biased quantum tunneling of magnetization in a rectangular $[Mn_3]_4$ tetramer†

Tu N. Nguyen,[a] Wolfgang Wernsdorfer,[b] Muhandis Shiddiq,[c] Khalil A. Abboud,[a] Stephen Hill[c] and George Christou*[a]

The syntheses and properties of four magnetically-supramolecular oligomers of triangular Mn_3 units are reported: dimeric $[Mn_6O_2(O_2CMe)_8(CH_3OH)_2(pdpd)_2]$ (**3**) and $[Mn_6O_2(O_2CMe)_8(py)_2(pdpd)_2](ClO_4)_2$ (**4**), and tetrameric $[Mn_{12}O_4(O_2CR)_{12}(pdpd)_6](ClO_4)_4$ (R = Me (**5**), ^{t}Bu (**6**)). They were all obtained employing 3-phenyl-1,5-di(pyridin-2-yl)pentane-1,5-dione dioxime ($pdpdH_2$), either in direct synthesis reactions involving oxidation of Mn^{II} salts or in metathesis reactions with the preformed complex $[Mn_3O(O_2CMe)_6(py)_3](ClO_4)$ (**1**); complex **6** was then obtained by carboxylate substitution on complex **5**. Complexes **3** and **4** contain two $[Mn^{III}_2Mn^{II}(\mu_3\text{-}O)]^{6+}$ and $[Mn^{III}_3(\mu_3\text{-}O)]^{7+}$ units, respectively, linked by two $pdpd^{2-}$ groups. Complexes **5** and **6** contain four $[Mn^{III}_3(\mu_3\text{-}O)]^{7+}$ units linked by six $pdpd^{2-}$ groups into a rectangular tetramer $[Mn^{III}_3]_4$. Solid-state dc magnetic susceptibility studies showed that the Mn_3 subunits in **3** and **4** have a ground-state spin of $S = 3/2$ and $S = 2$, respectively, while the Mn_3 subunits in **5** and **6** possess an $S = 6$ ground state. Complexes **5** and **6** exhibit frequency-dependent out-of-phase (χ''_M) ac susceptibility signals indicating **5** and **6** to be tetramers of Mn_3 single-molecule magnets (SMMs). High-frequency EPR studies of a microcrystalline powder sample of $\mathbf{5}\cdot 2CH_2Cl_2$ provided precise spin Hamiltonian parameters of $D = -0.33$ cm^{-1}, $|E| = 0.03$ cm^{-1}, $B^0_4 = -8.0 \times 10^{-5}$ cm^{-1}, and $g = 2.0$. Magnetization *vs.* dc field sweeps on a single crystal of $\mathbf{5}\cdot x CH_2Cl_2$ gave hysteresis loops below 1 K that exhibit exchange-biased quantum tunneling of magnetization (QTM) steps with a bias field of 0.19 T. Simulation of the loops determined that each Mn_3 unit is exchange-coupled to the two neighbors linked to it by the $pdpd^{2-}$ linkers, with an antiferromagnetic inter-Mn_3 exchange interaction of $J/k_B = -0.011$ K ($\hat{H} = -2J\hat{S}_i\cdot\hat{S}_j$ convention). The work demonstrates a rational approach to synthesizing magnetically-supramolecular aggregates of SMMs as potential multi-qubit systems for quantum computing.

Received 17th July 2015
Accepted 1st November 2015

DOI: 10.1039/c5sc02599k

www.rsc.org/chemicalscience

Introduction

Single-molecule magnets (SMMs) are individual molecules that function as single-domain nanoscale magnetic particles,[1,2,3,4,5] and they bring the advantages of molecular chemistry to the field of nanoscale magnetism, such as crystallinity, monodispersity, solubility, and a shell of organic ligands that can be readily varied. Different from molecule-based magnets, which require intermolecular interactions and long-range ordering,[6,7,8,9] SMMs are a class of metal clusters that display superparamagnetic behavior down to a characteristic blocking temperature, T_B, below which they exhibit slow magnetization dynamics. For Mn and most 3d transition metal SMMs, this behavior arises from the combination of a large ground-state spin (S) and Ising-type magnetoanisotropy (negative zero-field splitting parameter, D), which leads to a significant energy barrier to the thermal equilibration of the molecular magnetic moment. Experimentally, an SMM exhibits frequency-dependent out-of-phase ac magnetic susceptibility signals, and hysteresis in a plot of magnetization *vs.* applied dc magnetic field. The significant advantage of the single-molecule approach to nanomagnetism is the ability to investigate "particles" that are naturally identical and have well-defined sizes and electronic levels. Moreover, the possibility to modify the ligand sphere by standard solution chemistry methods allows for exquisite tuning of structures and magnetic properties of the molecules. Various families of SMMs have been discovered; the majority of which are Mn-based complexes with Mn_{84} being the largest among them.[10]

SMMs have also been shown to display interesting quantum phenomena such as quantum tunneling of magnetization

[a]*Department of Chemistry, University of Florida, Gainesville, Florida, 32611-7200, USA. E-mail: christou@chem.ufl.edu*

[b]*Institut Néel-CNRS, 38042 Grenoble Cedex 9, France*

[c]*National High Magnetic Field Laboratory and Department of Physics, Florida State University, Tallahassee, Florida, 32310, USA*

† Electronic supplementary information (ESI) available: Crystallographic details in CIF format, bond valence sums, bond distances and angles, structural figures, magnetic data, UV-vis spectra. CCDC 869139, 1413392, 1413393, 1413395. For ESI and crystallographic data in CIF or other electronic format see DOI: 10.1039/c5sc02599k

(QTM),[11,12] quantum phase interference (QPI),[13,14,15] spin–spin cross relaxation,[16] and quantum entanglement.[17,18,19] Consequently, they have been proposed as qubits for quantum computation[20–23] and as components in molecular spintronics devices,[24,25] which would exploit their quantum tunneling properties. For such applications, weak couplings of two or more SMMs to each other or to other components of a device are essential, while maintaining the intrinsic single-molecule properties of each SMM, and this represents the main goal of this study. The report of supramolecular C–H···Cl hydrogen-bonded pairs of $[Mn_4O_3Cl_4(O_2CEt)_3(py)_3]$ ($S = 9/2$) demonstrated such coupling between two SMMs for the first time, manifested as exchange-biased QTM steps, quantum superposition states, and quantum entanglement of the two SMMs.[17,18,19,26] Several supramolecular dimers, chains, and 3D networks of weakly coupled SMMs connected by hydrogen-bonds have since been reported.[27–33] Disadvantages of linkage by hydrogen-bonds, however, are (i) de-aggregation into monomeric units on dissolution, and (ii) the major loss of synthetic control, with all the previously mentioned supramolecular aggregates being discovered serendipitously. A superior approach is connection of SMMs *via* covalent bonds. Such covalent linkage of SMMs has already been explored extensively, invariably leading to chains or 2- or 3D networks.[34–50] Discrete, magnetically-supramolecular[51,52] oligomers of magnetic molecules comprising two or more covalently linked subunits are relatively rare.[53–64] Several studies have provided important insights into tailoring exchange interactions when connecting non-SMM subunits, such as the linking of two Cr_7Ni wheel molecules[65,66] or two lanthanide ions,[67,68,69,70,71] resulting in weak antiferromagnetic (AF) or ferromagnetic (F) interactions. Only a few of these exhibit SMM behavior and none display exchanged-biased QTM steps in hysteresis loops, probably due to the SMM subunits interacting too strongly causing the oligomer to behave magnetically like a single molecule,[54] or individual SMM subunits having low lying excited states that interfere with the quantum tunneling process, resulting in stepless hysteresis loops even when the interactions between the subunits are weak.[60]

An ideal magnetically-supramolecular aggregate of SMMs should possess two features: (i) each subunit is a 'good' SMM showing hysteresis loops with clear QTM steps; and (ii) the exchange-coupling through the connecting ligands is very weak so as to represent merely a small perturbation of the single-molecule properties of the constituent SMM subunits. Moreover, a better understanding can be achieved if the properties of the aggregate can be compared to those of the corresponding monomer from which it is constructed, thus requiring the SMM monomer to be available to function as a control for independent structural and magnetic characterization. The desired oligomers might be obtainable by direct synthesis from simple reagents but there are many potential problems and no guarantee that the desired magnetic properties will be obtained this way. A more rational and controllable route would be to apply a building-block approach of linking SMMs together using suitably-designed linker groups that will result in weak inter-SMM interactions, while ensuring that molecular oligomers rather than polymers are obtained.

Our group has therefore initiated a program to link covalently two or more SMMs to give non-polymeric, magnetically-supramolecular 'aggregates-of-SMMs' exhibiting very weak inter-SMM exchange interactions. The objective is to obtain materials exhibiting exchange-biased QTM and, in some cases, allow detailed study of quantum superposition states and related phenomena. For these reasons we are targeting small oligomers at this stage, in order to better detect the signatures of these nebulous and fragile effects. In the present work, we report the synthesis and properties of four oligomeric aggregates of Mn_3 units; two $[Mn_3]_2$ dimers and two $[Mn_3]_4$ tetramers, all containing dioximate inter-Mn_3 linker groups. We shall describe their structures and magnetic properties and, for one of the $[Mn_3]_4$ tetramers, the detailed analysis of high-frequency EPR and micro-SQUID magnetic data. Some preliminary results have been previously communicated.[72]

Experimental section

Syntheses

All manipulations were performed under aerobic conditions using chemicals and solvents as received unless otherwise stated. $[Mn_3O(O_2CMe)_6(py)_3](ClO_4)$ (**1**) was prepared as described elsewhere;[73] the dioxime $pdpdH_2$ was synthesized as previously reported.[72]

Caution! Although no such behavior was observed during the present work, perchlorate compounds are potentially explosive; such compounds should be synthesized and used in small quantities, and treated with utmost care at all times.

$[Mn_6O_2(O_2CMe)_8(pdpd)_2(MeOH)_2]$ (3)

A solution of $Mn(O_2CMe)_2\cdot 4H_2O$ (0.25 g, 1.0 mmol) in 15 mL of MeCN/MeOH (2 : 1 v/v) was treated with NEt_3 (0.14 mL, 1.0 mmol) and $pdpdH_2$ (0.18 g, 0.50 mmol). The solution was stirred for 1 hour at room temperature, filtered and the dark brown filtrate left undisturbed to concentrate slowly by evaporation. X-ray quality crystals of $\mathbf{3}\cdot x$MeOH$\cdot y$MeCN slowly formed over one week. These were collected by filtration, washed with Et_2O, and dried under vacuum. The yield was 75% based on Mn. Anal. calcd (found) % for $\mathbf{3}\cdot 4H_2O$ ($Mn_6O_{28}C_{60}H_{76}N_8$): C 42.72 (42.39); H 4.54 (4.18); N 6.64 (6.25). Selected IR data (KBr, cm^{-1}): 1600 (s), 1471 (m), 1397 (s), 1338 (m), 1182 (m), 1107 (w), 1035 (w), 784 (w), 760 (w), 700 (m), 658 (m), 614 (m), 542 (w), 421 (w).

$[Mn_6O_2(O_2CMe)_8(pdpd)_2(py)_2](ClO_4)_2$ (4)

A brown solution of complex **1** (0.44 g, 0.50 mmol) in 15 mL of MeCN/MeOH (2 : 1 v/v) was treated with $pdpdH_2$ (0.18 g, 0.50 mmol). The solution was stirred for 1 hour at room temperature and then evaporated under vacuum to obtain black powder. The powder was dissolved in CH_2Cl_2 (25 mL) and the resulting solution was layered with Et_2O (50 mL). X-ray quality crystals of $\mathbf{4}\cdot x Et_2O\cdot y CH_2Cl_2$ slowly formed over 2 days. The crystals were collected by filtration, washed with Et_2O and dried under vacuum. The yield was 80% based on Mn. Anal. calcd (found) % for $\mathbf{4}\cdot 3H_2O$ ($Mn_6O_{33}C_{68}H_{76}N_{10}Cl_2$): C 41.63 (41.79); H 3.90 (3.62); N 7.14 (6.77). Selected IR data (KBr, cm^{-1}): 1600 (s), 1474

(m), 1392 (s), 1339 (m), 1182 (w), 1108 (m), 1030 (w), 937 (w), 784 (w), 760 (w), 698 (w), 661(m), 625 (w).

$[Mn_{12}O_4(O_2CMe)_{12}(pdpd)_6](ClO_4)_4$ (5)

A brown solution of complex **1** (0.044 g, 0.050 mmol) in 25 mL of CH_2Cl_2 was treated with $pdpdH_2$ (0.036 g, 0.10 mmol). The solution was stirred for 1 hour at room temperature, filtered, and the black filtrate left undisturbed. X-ray quality crystals of $\mathbf{5}\cdot x CH_2Cl_2$ slowly formed over 2 days. The crystals were collected by filtration, washed with CH_2Cl_2 and dried under vacuum. The yield was 35% based on Mn. Anal. calcd (found) % for $\mathbf{5}\cdot 2CH_2Cl_2$ (ref. 74) ($Mn_{12}O_{56}C_{152}H_{148}N_{24}Cl_8$): C 43.99 (43.58); H 3.59 (3.54); N 8.10 (7.75). Selected IR data (KBr, cm^{-1}): 1600 (s), 1574 (s), 1474 (m), 1388 (s), 1337 (m), 1183 (m), 1162 (m), 1109 (s), 1088 (m), 1047(w), 781 (w), 758 (w), 700 (m), 661(m), 623 (m).

$[Mn_{12}O_4(O_2C^tBu)_{12}(pdpd)_6](ClO_4)_4$ (6)

A brown solution of complex **5** (0.21 g, 0.050 mmol) in 30 mL of MeCN : EtOH (2 : 1 v/v) was treated with pivalic acid (0.12 g, 1.2 mmol), and the solution was stirred overnight at room temperature. Toluene (10 mL) was added and the solvent was removed under vacuum. After three cycles of toluene addition and removal, the residue was dissolved in CH_2Cl_2 (25 mL) and the resulting solution was layered with hexanes (50 mL). X-ray quality crystals of $\mathbf{6}\cdot x CH_2Cl_2$ slowly formed over 3 days. The crystals were collected by filtration, washed with hexanes, and dried under vacuum. The yield was 50% based on Mn. Anal. calcd (found) % for $\mathbf{6}\cdot 2CH_2Cl_2$ (ref. 74) ($Mn_{12}O_{56}C_{188}H_{220}N_{24}Cl_8$) C 48.51 (48.83); H 4.76 (4.92); N 7.22 (6.95). Selected IR data (KBr, cm^{-1}): 1601 (s), 1584 (s), 1561 (s), 1516 (w), 1478 (s), 1440 (w), 1400 (s), 1384 (m), 1348 (s), 1219 (s), 1188 (m), 1165 (w), 1096 (s), 1083 (m), 756 (w), 700 (m), 663 (m), 622 (s), 449 (m).

X-ray crystallography

X-ray intensity data were collected at 100 K on a Bruker DUO diffractometer using MoK_α radiation (λ = 0.71073 Å) and an APEXII CCD area detector. Suitable crystals of $\mathbf{3}\cdot x MeOH\cdot y MeCN$, $\mathbf{4}\cdot x Et_2O\cdot y CH_2Cl_2$, $\mathbf{5}\cdot x CH_2Cl_2$ and $\mathbf{6}\cdot x CH_2Cl_2$ were attached to glass fibers using silicone grease and transferred to a goniostat where they were cooled to 100 K for data collection. Raw data frames were read by the program SAINT and integrated using 3D profiling algorithms. The resulting data were reduced to produce *hkl* reflections, their intensities and estimated standard deviations. The data were corrected for Lorentz and polarization effects, and numerical absorption corrections were applied based on indexed and measured faces. The structures were solved and refined in SHELXTL6.1,[75] using full-matrix least-squares refinement cycles. The non-H atoms were refined with anisotropic thermal parameters and all of the H atoms were calculated in idealized positions and refined as riding on their parent atoms. Unit cell data and structural refinement details for the four compounds are listed in Table 1. More details are provided in ESI.†[76]

Physical and spectroscopic measurements

Infrared spectra were recorded in the solid state (KBr pellets) on a Nicolet Nexus 670 FTIR spectrometer in the 400–4000 cm^{-1} range. Elemental analyses (C, H, and N) were performed by the in-house facilities of the University of Florida, Chemistry Department. Variable-temperature direct current (dc) and alternating current (ac) magnetic susceptibility data were collected at the University of Florida using a Quantum Design MPMS-XL SQUID magnetometer equipped with a 7 T magnet and operating in the 1.8–300 K range. Samples were embedded in solid eicosane to prevent torquing. Magnetization *vs.* field and temperature data were fit using the program MAGNET.[77a] Pascal's constants were used to estimate the diamagnetic

Table 1 Crystal data and structure refinement parameters for complexes **3–6**

Parameter	$\mathbf{3}\cdot x MeOH\cdot y MeCN$	$\mathbf{4}\cdot x C_4H_{10}O\cdot y CH_2Cl_2$	$\mathbf{5}\cdot x CH_2Cl_2$	$\mathbf{6}\cdot x CH_2Cl_2$
Formula[a]	$C_{65}H_{86}Mn_6N_{10}O_{26}$	$C_{82}H_{98}Cl_{10}Mn_6N_{10}O_{32}$	$C_{150.25}H_{144}Cl_{4.50}Mn_{12}N_{24}O_{56}$	$C_{206}H_{252}Cl_{44}Mn_{12}N_{24}O_{48}$
FW[a], g mol^{-1}	1753.08	2419.84	4000.70	6051.40
Crystal system	Monoclinic	Triclinic	Monoclinic	Monoclinic
Space group	$C_{2/c}$	$P\bar{1}$	$P_{21/c}$	$C_{2/c}$
a, Å	16.0232(17)	16.7797(18)	34.190(4)	42.112(3)
b, Å	41.093(4)	16.9615(18)	32.890(4)	26.4980(16)
c, Å	13.0506(14)	20.538(4)	44.013(5)	30.5334(18)
α, °	90	93.849(3)	90	90
β, °	110.908(2)	105.068(3)	110.320(3)	127.707(1)
γ, °	90	116.263(2)	90	90
V, $Å^3$	8027.2(15)	4948.4(11)	46 413(9)	26 956(3)
Z	4	2	8	4
T, K	100(2)	100(2)	100(2)	100(2)
λ, Å[b]	0.71073	0.71073	0.71073	0.71073
ρ_{calc}, g cm^{-3}	1.451	1.624	1.145	1.491
μ, mm^{-1}	0.995	1.097	0.748	1.048
R_1[c,d]	0.0460	0.0732	0.0740	0.0505
wR_2[e]	0.1276	0.2028	0.1617	0.1218

[a] Including solvate molecules. [b] Graphite monochromator. [c] $I > 2\sigma(I)$. [d] $R_1 = \sum(||F_o| - |F_c||)/\sum|F_o|$. [e] $wR_2 = [\sum[w(F_o^2 - F_c^2)^2]/\sum[w(F_o^2)^2]]^{1/2}$ where $w = 1/[\sigma^2(F_o^2) + (m \times p)^2 + n \times p]$, $p = [\max(F_o^2, 0) + 2 \times F_c^2]/3$, *m* and *n* are constants.

correction, which was subtracted from the experimental susceptibility to give the molar paramagnetic susceptibility (χ_M). Low-temperature (<1.8 K) hysteresis loop and dc relaxation measurements were performed at Institut Néel using an array of micro-SQUIDS.[78] The high sensitivity of this magnetometer allows the study of single crystals of SMMs of the order of 10–500 μm. The field can be applied in any direction by separately driving three orthogonal coils. High-frequency EPR (HF-EPR) powder spectra were collected at the Electron Magnetic Resonance facility of the U.S. National High Magnetic Field Laboratory using a broadband (10 to 700 GHz) transmission probe in which microwaves are propagated into and out of a 17 T superconducting magnet through cylindrical light pipes.[79] Tunable microwave radiation was generated using a phase-locked Virginia Diodes solid-state source operating at 13 ± 1 GHz, followed by a chain of solid-state multipliers and amplifiers. Field modulation was employed in conjunction with a phase-sensitive homodyne detection scheme using a cold bolometer, yielding derivative mode spectra. Temperature control was achieved using helium gas flow cryostats.

Results and discussion

Syntheses

The synthetic strategies employed in this work are based on the report in 2007 that the use of the mono-oxime methyl-2-pyridyl ketone oxime (mpkoH; Fig. 1) in Mn^{III} carboxylate chemistry gives the triangular complex $[Mn_3O(O_2CMe)_3(mpko)_3](ClO_4)$ (**2**), which has an $S = 6$ ground state and is an SMM.[80] The cation of **2** has C_3 symmetry with the acetate and $mpko^-$ ligands on opposite sides of the Mn_3 plane (Fig. 1). This tripodal arrangement of the three oximates made this Mn_3 SMM attractive to us for our present objectives because it suggested that their replacement with dioximates to link multiple Mn_3 units together might give molecular oligomers rather than polymers.

After some planning, we settled on the dioxime 3-phenyl-1,5-di(pyridin-2-yl)pentane-1,5-dione dioxime ($pdpdH_2$) for this work. It was designed taking into consideration the established binding modes of mpkoH, which has been well investigated in transition metal chemistry by many groups,[81–89] and the decision to have a three-carbon linker between the two ends to impart sufficient length and flexibility to yield any potential oligomeric product without steric problems. The Ph ring at the central carbon atom was included to facilitate the synthesis, which comprised the reaction of two equivalents of 2-acetylpyridine with benzaldehyde to give the dione[90] followed by a standard conversion to the dioxime with hydroxylamine. We recognized that the overall flexibility of $pdpdH_2$ meant that it was not 'pre-programmed' to yield any particular degree of oligomerization or product topology, but this was as desired at this initial stage in order to explore various possibilities.

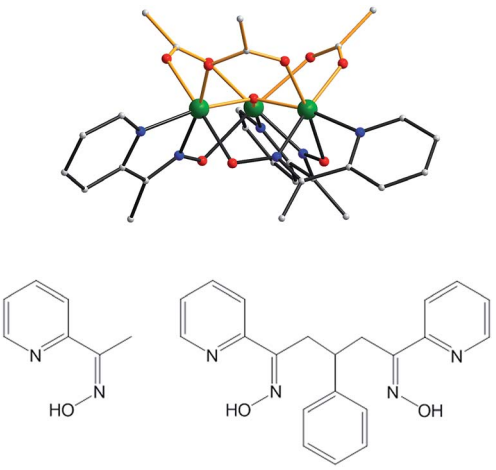

Fig. 1 Structure of the cation of complex **2** (top), mpkoH (bottom left) and $pdpdH_2$ (bottom right). Colour code: Mn green; N blue; O red; C grey.

Two procedures to **2** had been used[80] that could now be employed with $pdpdH_2$: (i) direct synthesis with simple reagents involving comproportionation between Mn^{II} acetate and MnO_4^- in a 3 : 1 ratio in the presence of $MeCO_2H$ and mpkoH, the Mn^{3+} : Mn^{7+} ratio of 3 : 1 giving a $Mn^{3.25+}$ average; and (ii) reaction of mpkoH with the non-SMM $[Mn_3O(O_2CMe)_6(py)_3](ClO_4)$ (**1**) in a 3 : 1 ratio (eqn (1)). Analogues of **2** with other carboxylates were also available from these methods using the corresponding starting materials.

$$[Mn_3O(O_2CR)_6(py)_3]^+ + 3mpkoH \rightarrow [Mn_3O(O_2CR)_3(mpko)_3]^+ + 3RCO_2H + 3py \quad (1)$$

The reactions between $pdpdH_2$ and a series of manganese salts were screened under a variety of conditions: solvent, stoichiometry, presence or absence of base, *etc.* Reaction of $Mn(O_2CMe)_2$, $pdpdH_2$ and NEt_3 in a 2 : 1 : 2 molar ratio in MeCN : MeOH (2 : 1 v/v) led to $[Mn_6O_2(O_2CMe)_8(pdpd)_2(MeOH)_2]$ (**3**) (eqn (2)).

The oxidation of Mn^{II} to Mn^{III} is by atmospheric O_2, facilitated by the basic conditions imparted by the NEt_3. In the absence of NEt_3, the reaction is much slower and the yield of **3** is much lower. The Mn^{II} : $pdpdH_2$ reaction ratio of 2 : 1 means the dioxime is in excess, but reactions with 3 : 1 still gave the same product in comparable yield. The cleanest, most crystalline product was obtained with the 2 : 1 ratio, as in the Experimental section.

$$6Mn(O_2CMe)_2 + 2pdpdH_2 + 2MeOH + 4NEt_3 + O_2 \rightarrow [Mn_6O_2(O_2CMe)_8(pdpd)_2(MeOH)_2] + 4MeCO_2^- + 4Et_3NH^+ + 4H_2O \quad (2)$$

3 is mixed-valence ($2Mn^{II}$, $4Mn^{III}$) indicating incomplete oxidation of Mn^{II} under these conditions. To explore whether an all-Mn^{III} analogue was obtainable, we used the preformed Mn^{III} complex **1**. Indeed, the 1 : 1 reaction of $pdpdH_2$ with **1** in MeCN : MeOH (2 : 1 v/v) successfully gave $[Mn_6O_2(O_2CMe)_8(pdpd)_2(py)_2](ClO_4)_2$ (**4**), the all-Mn^{III} version of **3** (eqn (3)). In both **3** and **4**, each $pdpd^{2-}$ oxime group clips onto the same edge of each of the two Mn_3 triangular units, the other edges being bridged by only acetate groups (*vide infra*).[80]

$$2[Mn_3O(O_2CMe)_6(py)_3]^+ + 2pdpdH_2 \rightarrow [Mn_6O_2(O_2CMe)_8(py)_2(pdpd)_2]^{2+} + 4MeCO_2^- + 4pyH^+ \quad (3)$$

We now turned our attention to obtaining analogues of **2** with dioximate linkers bound to all edges of the triangular core rather than mpko$^-$. Given our observations with **3** and **4**, we decided to employ preformed **1** rather than Mn^{II} salts. Thus, the 1 : 2 reaction of **1** and $pdpdH_2$ in CH_2Cl_2 was explored and this led to $[Mn_{12}O_4(O_2CMe)_{12}(pdpd)_6]^{4+}$ (**5**) (eqn (4)).

$$4[Mn_3O(O_2CMe)_6(py)_3]^+ + 6pdpdH_2 \rightarrow [Mn_{12}O_4(O_2CMe)_{12}(pdpd)_6]^{4+} + 12MeCO_2^- + 12pyH^+ \quad (4)$$

The excess of $pdpdH_2$ was beneficial, the stoichiometric 2 : 3 ratio of eqn (4) giving a much lower yield. Ratios higher than 1 : 2 did not improve the yield further. The CH_2Cl_2 solvent was crucial for obtaining good crystals, the MeCN : MeOH (2 : 1 v/v) medium, as used for **3** and **4**, also giving **5** but as crystals unsuitable for crystallography.

With **5** attained and characterized (*vide infra*), it was of importance for the magnetic studies to determine if its ligation could be modified in a controlled fashion. We have previously shown that the acetate groups of, for example, the $[Mn_{12}O_{12}(O_2CMe)_{16}(H_2O)_4]$ SMM can be substituted with numerous other carboxylates,[5] the substitution being driven to completion by removal of $MeCO_2H$ as its toluene azeotrope under vacuum. This controlled modification has been crucial for many studies on SMMs.[91–97] We have now found that a similar carboxylate substitution using pivalic acid is possible for **5**, without breaking any of the dioximate linkages, to give **6** (eqn (5)). This mild carboxylate substitution augurs well that controlled modification of supramolecular aggregates of many types will be possible in the future to optimize them for particular studies or attachment to functional units or surfaces.

$$[Mn_{12}O_4(O_2CMe)_{12}(pdpd)_6]^{4+} + 12^tBuCO_2H \rightarrow [Mn_{12}O_4(O_2C^tBu)_{12}(pdpd)_6]^{4+} + 12MeCO_2H \quad (5)$$

Description of structures

The structures of **3** and the cation of **4** are shown in Fig. 2 and 3, and selected interatomic distances and angles are listed in ESI.†[76] The compounds are essentially isostructural. Their cores (Fig. 3) consist of two $[Mn^{II}Mn^{III}_2(\mu_3\text{-}O)]^{6+}$ (**3**) or $[Mn^{III}_3(\mu_3\text{-}O)]^{7+}$ (**4**) triangular subunits linked by two $pdpd^{2-}$ groups to give $[Mn_3]_2^{0/2+}$ dimers. The O^{2-} ions lie only slightly out of the Mn_3 planes in both complexes (d = 0.002–0.017 Å). Interestingly, both $pdpd^{2-}$ linkers attach to the same Mn_3 edge so that these edges are bridged by two pyridyloximate groups whereas the other edges are bridged by two acetate groups each. This is distinctly different from **2** (Fig. 1) where each edge is bridged by one mpko$^-$ and one acetate. The ligation is completed by terminal MeOH groups on the Mn^{II} atoms (Mn_3, Mn_3') in **3** and pyridine groups on the Mn^{III} ions at the corresponding positions in **4**. The Mn oxidation states were deduced from charge balance considerations and the Mn^{III} Jahn–Teller distortions

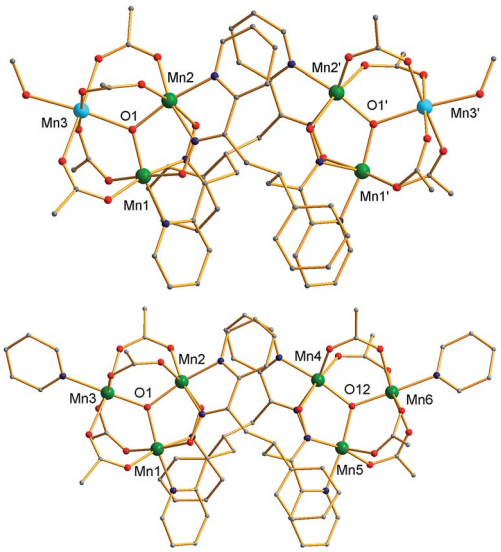

Fig. 2 Complete structure of **3** (top) and the cation of **4** (bottom) with H atoms omitted for clarity. Colour code: Mn^{III} green; Mn^{II} sky blue; O red; N blue; C grey.

(Fig. 3), and confirmed by bond valence sum (BVS) calculations. BVS calculations also confirmed that the μ_3-O atoms are O^{2-} ions.[76]

The Mn_3 triangles are far from equilateral, with Mn···Mn separations and Mn–O^{2-}–Mn angles for the edges bridged by two oximate groups being noticeably smaller than those for edges bridged by two acetates. This is a characteristic of a diatomic N–O oximate bridge *vs.* a triatomic O–C–O carboxylate bridge. The triangles are crystallographically scalene but isosceles within the 3σ criterion. Overall, both dimers have C_2 symmetry, either crystallographic (**3**) or virtual (**4**). Inspection of short contacts reveals that each $[Mn_3]_2$ dimer molecule of **3** connects to two neighbors by two hydrogen-bonds to each ($O_{acet}\cdots O_{MeOH}$ = 2.752(4) Å) to form a $\{[Mn_3]_2\}_n$ zig-zag chain (Fig. S1†).[76]

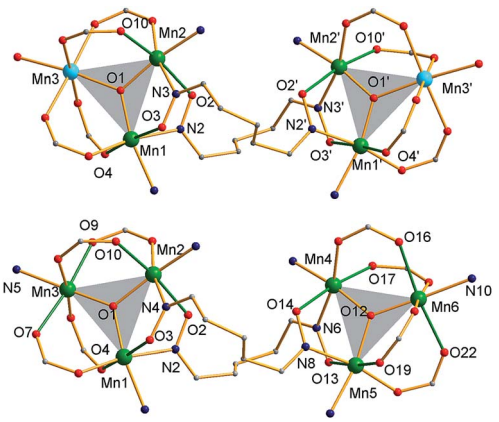

Fig. 3 The cores of **3** (top) and the cation of **4** (bottom) emphasizing the inter-Mn_3 connectivity, the Mn_3 planes (grey triangles), and Jahn–Teller axes (green bonds). Colour code: Mn^{III} green; Mn^{II} sky blue; O red; N blue; C grey.

The structure of the cation of **5** is shown in Fig. 4. The cation of **6** (Fig. S2†) is very similar and will not be described separately. Selected $[Mn_3(\mu_3\text{-}O)]$ core distances and angles for the cation of **5** are listed in Table 2, and fuller listings for both cations are available in ESI.†[76] The asymmetric unit of **5** consists of two essentially superimposable $[Mn_3]_4^{4+}$ cations (only the one shown in Fig. 4 will be discussed further), eight ClO_4^- anions, and large amounts of disordered CH_2Cl_2 solvent; the asymmetric unit of **6** contains only one cation. The cation consists of four $[Mn_3(\mu_3\text{-}O)]^{7+}$ units linked by six $pdpd^{2-}$ groups to give a rectangular $[Mn_3]_4$ supramolecule with each Mn_3 unit at a corner. One of the two μ-$MeCO_2^-$ ligands bridging each edge of **1** has been replaced by a bridging oximate from a $pdpd^{2-}$ group. The long and short sides of the rectangle are bridged by one and two $pdpd^{2-}$ groups, respectively (Fig. 4). In addition, the $pdpd^{2-}$ pyridyl groups have replaced the terminal pyridine ligands of **1**. Each of the μ_3-O^{2-} ions lies slightly above the Mn_3 plane ($d \sim 0.3$ Å), and all the Mn–N–O–Mn torsion angles are relatively large ($\phi \sim 8$–$20°$) (Table 3), as in **2**. Thus, the local structure of each Mn_3 unit of **5** (and **6**) is very similar to that of **2**. Also as in **2**, the three bridging oximate groups are on the same side of the Mn_3 plane, and this facilitates the formation of a molecular tetramer rather than a polymer. The flexibility of $pdpd^{2-}$, however, is likely why a rectangular rather than tetrahedral $[Mn_3]_4$ topology, as might be expected from four tripodal

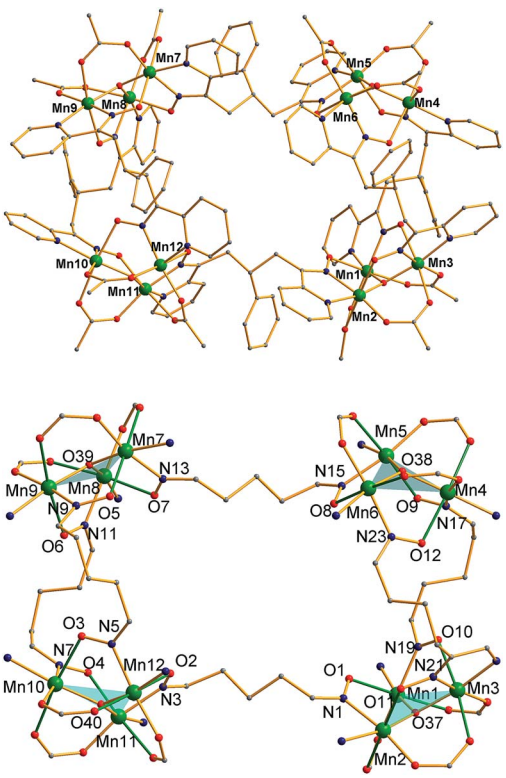

Fig. 4 (Top) complete molecular structure of the cation of **5** with H atoms omitted for clarity; (bottom) the core emphasizing the connectivity, orientation of the Mn_3 planes (blue triangles), and the Jahn–Teller axes (green bonds). Colour code: Mn^{III} green; O red; N blue; C grey.

Table 2 Selected $[Mn_3(\mu_3\text{-}O)]$ core distances (Å) and angles (°) in the cation of **5**

	Distance (Å)		Angle (°)
Mn1···Mn3	3.184(2)	Mn1–O37–Mn3	115.3(2)
Mn1···Mn2	3.212(2)	Mn1–O37–Mn2	118.3(3)
Mn2···Mn3	3.201(2)	Mn2–O37–Mn3	118.6(3)
Mn4···Mn5	3.189(2)	Mn4–O38–Mn5	116.5(3)
Mn4···Mn6	3.173(2)	Mn4–O38–Mn6	116.9(3)
Mn5···Mn6	3.216(2)	Mn5–O38–Mn6	118.2(3)
Mn7···Mn8	3.180(2)	Mn7–O39–Mn8	116.3(3)
Mn7···Mn9	3.206(2)	Mn7–O39–Mn9	118.0(3)
Mn8···Mn9	3.205(2)	Mn8–O39–Mn9	118.7(3)
Mn10···Mn11	3.185(2)	Mn10–O40–Mn11	118.5(3)
Mn10···Mn12	3.197(2)	Mn10–O40–Mn12	116.6(3)
Mn11···Mn12	3.218(2)	Mn11–O40–Mn12	119.3(3)

units and stiff linkers, has been obtained. The elemental analysis data for vacuum-dried **5** and **6** both indicate two CH_2Cl_2 molecules, and this is consistent with the observation of two CH_2Cl_2 molecules encapsulated within the central cavity of the Mn_{12} cations, with no opening big enough for them to escape (Fig. S3†).[74]

As seen also for **2**, the Mn···Mn separations and Mn–O^{2-}–Mn angles span a small range and lead to each triangle being virtually isosceles within the 3σ criterion. Interestingly, both types of distortion from equilateral to isosceles are seen, *i.e.*, short/long/long and short/short/long Mn···Mn separations, and corresponding small/large/large and small/small/large Mn–O–Mn angles. There are two of each type of Mn_3 unit in the cation in Fig. 4 and Table 2. The Mn^{III} oxidation states were confirmed by BVS calculations, and their JT elongation axes (green bonds in Fig. 4) are aligned in a propeller fashion, again as in **2**. Overall, the cations of both **5** and **6** have virtual D_{2d} symmetry, *i.e.*, the four Mn_3 units are virtually symmetry equivalent.

Magnetochemistry

Direct current magnetic susceptibility studies. In addition to general magnetic characterization of **3–6**, there were two crucial questions targeted at **5** (and **6**) that needed to be addressed: (i) is each Mn_3 subunit still an SMM with $S = 6$, or has the aggregation altered the properties *vs.* **2**? and (ii) is there any evidence for weak inter-Mn_3 interactions within the $[Mn_3]_2$ tetramer? Variable-temperature, direct current (dc) magnetic susceptibility (χ_M) measurements were performed on vacuum-dried polycrystalline samples of **3–6** in an applied field of 1000 G (0.10 T) and in the 5.0–300 K temperature range. The samples were restrained in eicosane to prevent torquing. The data for $\mathbf{3}\cdot 4H_2O$ and $\mathbf{4}\cdot 3H_2O$ are shown as $\chi_M T$ *vs.* T in Fig. 5. $\chi_M T$ for $\mathbf{3}\cdot 4H_2O$ is 15.51 cm^3 K mol^{-1} at 300 K, and steadily decreases with decreasing temperature to 3.32 cm^3 K mol^{-1} at 5.0 K. $\mathbf{4}\cdot 3H_2O$ displays a similar behavior, with a $\chi_M T$ of 19.76 cm^3 K mol^{-1} at 300 K, decreasing to 5.31 cm^3 K mol^{-1} at 5.0 K. Interactions between the Mn_3 subunits are expected to be very weak, and thus the $\chi_M T$ at 300 K for $\mathbf{3}\cdot 4H_2O$, which is much smaller than the spin-only ($g = 2$) value for four Mn^{III} and two Mn^{II}

Table 3 Selected structural parameters for the [$Mn_3(\mu_3$-O) triangles of **5** and **6**

Complex **5**				Complex **6**			
Triangle	d^a	Torsion angle^b	ϕ (°)	Triangle	d^a	Torsion angle^b	ϕ (°)
Mn1Mn2Mn3	0.31	Mn1–N19–O10–Mn3	17.98	Mn1Mn2Mn3	0.31	Mn1–N2–O3–Mn3	14.38
		Mn2–N1–O1–Mn1	14.49			Mn2–N4–O4–Mn1	10.60
		Mn3–N21–O11–Mn2	10.90			Mn3–N6–O5–Mn2	13.30
Mn4Mn5Mn6	0.32	Mn4–N17–O9–Mn5	19.82	Mn4Mn5Mn6	0.31	Mn5–N10–O7–Mn4	18.31
		Mn5–N15–O8–Mn6	10.75			Mn6–N12–O8–Mn5	12.64
		Mn6–N28–O12–Mn4	18.28			Mn4–N8–O6–Mn6	10.96
Mn7Mn8Mn9	0.29	Mn7–N13–O7–Mn8	15.88				
		Mn8–N11–O6–Mn9	9.97				
		Mn9–N9–O5–Mn7	15.73				
Mn10Mn11Mn12	0.26	Mn10–N7–O4–Mn11	15.57				
		Mn11–N3–O2–Mn12	8.09				
		Mn12–N5–O3–Mn10	12.59				

^{a} Displacement (Å) of μ_3-oxide atom from the Mn_3 plane. ^{b} Mn–N–O–Mn torsion angle ϕ (°).

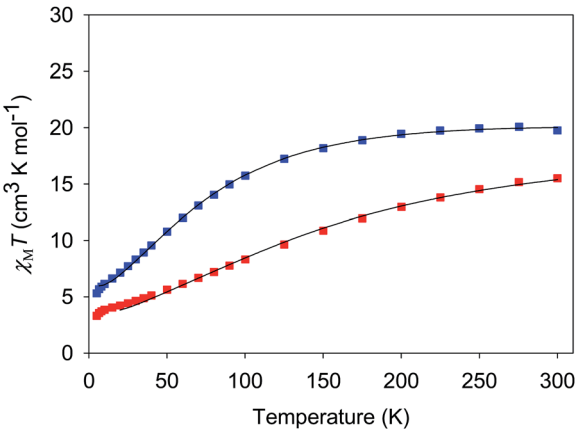

Fig. 5 $\chi_M T$ *vs.* T for complexes **3**·4H_2O (red) and **4**·3H_2O (blue). The solid lines are the fits of the data from 20–300 K (**3**) and 6.5–300 K (**4**); see Table 4 for the fit parameters.

non-interacting ions (20.75 cm^3 K mol^{-1}), indicates dominant or wholly antiferromagnetic (AF) interactions within the Mn_3 subunits. Complex **4**, however, has $\chi_M T$ value at 300 K slightly higher than the spin-only ($g = 2$) value for six Mn^{III} non-interacting ions ($\chi_M T = 18.00$ cm^3 K mol^{-1}), which together with the overall profile of the plot indicates both ferromagnetic (F) and AF interactions. The 5.0 K values are consistent with dimers of essentially non-interacting $S = 3/2$ and $S = 2$ subunits for **3** and **4**, respectively, with g slightly less than 2.0; the spin-only values would be 3.75 cm^3 K mol^{-1} and 6.00 cm^3 K mol^{-1}, respectively. In both cases, any inter-Mn_3 interactions would only contribute to the $\chi_M T$ decreases barely visible at the lowest T.

The $\chi_M T$ *vs.* T plots for **5**·2CH_2Cl_2 and **6**·2CH_2Cl_2 are essentially identical (Fig. 6), as expected from their near-identical structures. $\chi_M T$ for **5**·2CH_2Cl_2 increases from 48.25 cm^3 K mol^{-1} at 300 K to a plateau value of 76.55 cm^3 K mol^{-1} at 20 K, and then decreases slightly to 70.62 cm^3 K mol^{-1} at 5.0 K. For **6**·2CH_2Cl_2, $\chi_M T$ is 46.34 cm^3 K mol^{-1} at 300 K, increasing to 76.57 cm^3 K mol^{-1} at 25 K before slightly decreasing to 70.97 cm^3 K mol^{-1} at 5.0 K. The overall profiles are extremely similar to that of monomer **2**, indicating each of the four Mn_3 units of **5** and **6** to still be ferromagnetically coupled with $S = 6$ ground states. Indeed, the 300 K values of **5**·2CH_2Cl_2 and **6**·2CH_2Cl_2 are much larger than the spin-only ($g = 2$) value for twelve Mn^{III} atoms (36 cm^3 K mol^{-1}), and the peak values are as expected for four ostensibly non-interacting $S = 6$ units with g slightly less than 2.0 (spin-only value 84 cm^3 K mol^{-1}). The decreases below 20 K can be attributed to zero-field splitting (ZFS) within the $S = 6$ ground states, weak inter-Mn_3 interactions, and any Zeeman effects from the applied field.

The data were fit to the theoretical $\chi_M T$ *vs.* T expressions to obtain the exchange interaction parameters (J_{ij}) between Mn_i-Mn_j pairs. We assumed the interaction through the bridging pdpd^{2-} to be too weak to affect the data except at the lowest temperatures, and thus fit the data assuming non-interacting Mn_3 units; however, the H-bonding between different dimers of **3** should give somewhat stronger inter-Mn_3 interactions (*vide infra*). For complexes **3**/**4** and **5**/**6**, the theoretical $\chi_M T$ is the sum for two and four independent Mn_3 units, respectively. In accord

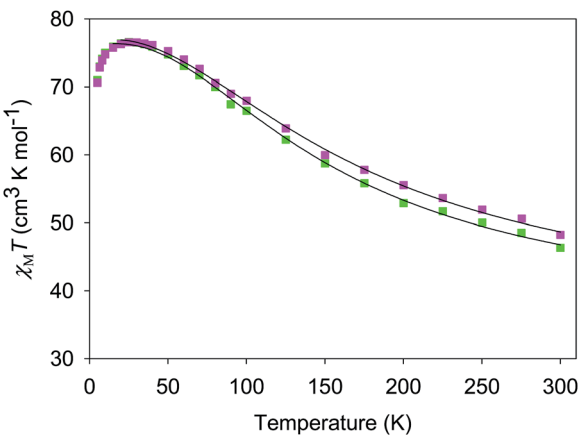

Fig. 6 $\chi_M T$ *vs.* T for complexes **5** (purple) and **6** (green). The solid lines are the fits of the data from 20–300 K (**5**) and 10–300 K (**6**); see Table 4 for the fit parameters.

with the mixed-valence nature of **3** and the Mn_3 structural parameters for **4–6**, we used an isosceles triangle model for each Mn_3 unit. For convenience, we label this triangle in a general way as Mn1Mn2Mn2′, with Mn2Mn2′ being the unique edge. The Heisenberg–Dirac–van Vleck (HDVV) spin Hamiltonian is then given by eqn (6), where $J = J_{12} = J_{12'}$ and $J' = J_{22'}$. Using the

$$\hat{H} = -2J(\hat{S}_1 \cdot \hat{S}_2 + \hat{S}_1 \cdot \hat{S}_{2'}) - 2J'\hat{S}_2 \cdot \hat{S}_{2'} \quad (6)$$

substitutions $\hat{S}_A = \hat{S}_2 + \hat{S}_{2'}$ and $\hat{S}_T = \hat{S}_A + \hat{S}_1$,[98] where $\hat{S}_T$ is the total spin of the Mn_3, the spin Hamiltonian becomes that in eqn (7). The eigenvalues are given in eqn (8), where $E(S_T, S_A)$ is the energy of state S_T arising

$$\hat{H} = -J(\hat{S}_T{}^2 - \hat{S}_A{}^2 - \hat{S}_1{}^2) - J'(\hat{S}_A{}^2 - \hat{S}_2{}^2 - \hat{S}_{2'}{}^2) \quad (7)$$

$$E(S_T, S_A) = -J[S_T(S_T + 1) - S_A(S_A + 1)] - J'[S_A(S_A + 1)] \quad (8)$$

from S_A. For **3**, $S_1 = 5/2$, $S_2 = S_{2'} = 2$, and S_T ranges from 1/2 to 13/2. For **4–6**, $S_1 = S_2 = S_{2'} = 2$, and S_T ranges from 0 to 6. A theoretical $\chi_M T$ *vs.* T expression was derived from the use of the van Vleck equation[99,76] and addition of a temperature-independent paramagnetism (TIP) term, which was kept constant at 100×10^{-6} cm^3 K mol^{-1} per Mn. The data at the lowest T were omitted because they were affected by factors not included in eqn (6), particularly the inter-dimer H-bonding in **3** (*vide supra*). The obtained fits ($R^2 > 0.99$) are shown as solid lines in Fig. 5 and 6, and the fit parameters are collected in Table 4. For **4**, **5** and **6**, there are at least two crystallographically inequivalent Mn_3 subunits, and the J and J' are to be taken as average values.

For both **3** and **4**, J and J' are AF and F, respectively. The J *vs.* J' error surfaces for the fits, obtained with the program GRID,[77b] showed them to be unique (Fig. S5 and S6†).[76] The obtained J and J' reveal **3** to have an $S = 3/2$ ground state with an $S = 5/2$ first excited state at 49.7 cm^{-1}. **4** has an $S = 2$ ground state and an $S = 3$ first excited state at 29.6 cm^{-1}. The presence of both F and AF interactions is as expected from the structures of **3** and **4**. The bis-acetate-bridged edges correspond to the AF J interactions, while the bis-oximate-bridged edge corresponds to the F J' interaction. This is consistent with previous studies of (i) $[Mn_3O(O_2CR)_6L_3]^{0,+}$ complexes ($2Mn^{III}Mn^{II}$ and $3Mn^{III}$),[73] where all couplings are AF, and (ii) mono-oximate bridged **2**, where all couplings are F.[80] In **3** and **4**, two oximates now bridge the J' (Mn^{III}_2) edge and the coupling is again F, consistent with the non-zero oximate Mn–O–N–Mn torsion angles in **3** (av 17.1°) and **4** (av 15.7°), one of the recognized effects that promote F coupling between Mn^{III} atoms.[100,101] Interestingly, on conversion of the Mn^{II} atoms in **3** to Mn^{III} in **4**, and the shortening of the resulting Mn–O^{2-} bond, the J' coupling increases by nearly a factor of three even though its Mn–O–N–Mn torsion angles decrease to 15.7°. This emphasizes the importance of not just the torsion angles but also of perturbations to coupling pathways through the central O^{2-} ion to the overall F J' coupling in **3** and **4**, and other O^{2-}-bridged Mn_3 triangles, as we have discussed elsewhere.[102]

For **5** and **6**, both J and J' are F. However, the error surface for **5** in Fig. 7 (and for **6** in Fig. S8†) show two minima of near-equivalent quality located either side of the J *vs.* J' line. These two minima are assigned to the two different distortions from equilateral to isosceles, as discussed above. Since the crystal structure of the cation of **5** shows that both distortions are present, we conclude that both J/J' pairs are present and contribute to the observed magnetic properties. In our previous study of monomer **2** and its other carboxylate analogues,[80] only one type of isosceles triangle was observed crystallographically and therefore only the best fit J/J' pairs were reported ($J = 12.1$–18.6 cm^{-1} and $J' = 1.5$–6.7 cm^{-1}), which are very similar to one of the fits in the present work.[80] Further, the two fits for **5** and **6** each have the same average within the fit uncertainties: $J_{av} = 11.8 \pm 0.1$ cm^{-1} for **5**, and $J_{av} = 10.3 \pm 0.1$ cm^{-1} for **6**. In all cases, the Mn_3 units have an $S = 6$ ground state, with an $S = 5$ first excited state. The first excited states lie 79.5 and 84.1 cm^{-1} above the ground states of **5** and **6**, respectively, and the ground states are thus well-isolated.

The ground states of the Mn_3 units in **5** and **6** were confirmed by fits of magnetization (M) data collected in the 0.1–7 T and 1.8–10 K ranges. The data, plotted as $M/N\mu_B$ *vs.* H/T in Fig. S9† (N is Avogadro's number and μ_B is the Bohr magneton) were fit, as described for **2**,[80] using the program MAGNET[77a] by diagonalization of the spin Hamiltonian matrix assuming only the ground state is populated, incorporating axial anisotropy ($D\hat{S}_z{}^2$) and Zeeman terms, and employing a full powder average.[103,104] We assumed each Mn_3 to be acting independently, *i.e.*, that any

Table 4 Fit parameters for the fits of $\chi_M T$ *vs.* T data for **3–6**

Complex	J (cm^{-1})	J' (cm^{-1})	g	S
3·4H$_2$O	−9.9 ± 0.5	10.4 ± 3.9	1.96 ± 0.04	3/2
4·3H$_2$O	−4.9 ± 0.1	28.4 ± 2.0	1.99 ± 0.01	2
5·2CH$_2$Cl$_2$	16.8 ± 0.6	1.5 ± 0.7	1.91 ± 0.01	6
	7.2 ± 0.7	21.4 ± 0.6		6
6·2CH$_2$Cl$_2$	13.5 ± 0.8	3.8 ± 1.0	1.91 ± 0.01	6
	6.8 ± 1.0	17.6 ± 0.8		6

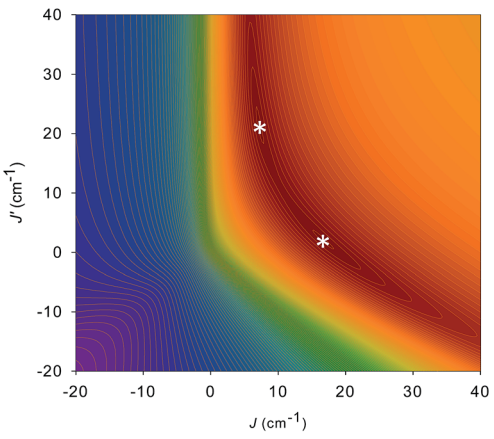

Fig. 7 2-D contour plot of the error surface for the J *vs.* J' fit of the dc $\chi_M T$ *vs.* T data for complex **5**. The darkest-brown region has the lowest error, where the two fits (asterisks) of comparable quality are located, and the blue region has the highest error. See Table 4 for the fit parameters.

inter-Mn_3 interactions through $pdpd^{2-}$ linkers were too weak to have a noticeable effect at these fields and temperatures. In support of the latter, we obtained excellent fits with $S = 6$, $g = 1.92(1)$, $D = -0.30(2)$ cm^{-1} for **5** and $S = 6$, $g = 1.89(1)$, $D = -0.30(2)$ cm^{-1} for **6**. These are very similar to those for **2** ($S = 6$, $D = -0.34$ cm^{-1}, and $g = 1.92$). The g *vs.* D error surfaces (Fig. S10†) revealed alternative fits with positive D but of much poorer quality.

Alternating current (ac) magnetic susceptibility studies. Ac magnetic susceptibility measurements were performed in the 1.8–15 K range in a 3.5 G ac field oscillating at 5–1000 Hz. The in-phase (χ'_M, plotted as $\chi'_M T$) and out-of-phase (χ''_M) ac susceptibility data for **5** are shown in Fig. 8; those for **3**, **4** and **6** are in Fig. S11–S13.† In each case, the data at >10 K or so are in agreement with the ground state S values deduced from the dc fits, providing independent support for those conclusions. For **5**, for example, the near-plateau $\chi'_M T$ of ~75 cm^3 K mol^{-1} is in good agreement with the dc peak value and is as expected for four $S = 6$ Mn_3 units with $g < 2.0$ (spin-only value 4×21 cm^3 K mol^{-1}). At lower T, $\chi'_M T$ drops due to zero-field splitting and any inter-Mn_3 interactions. Below 2.5 K, a characteristic frequency-dependent drop due to slow magnetization relaxation of a SMM is observed, and out-of-phase χ''_M signals are seen. This is very similar to the behaviour previously observed for monomer **2**. For **3** and **4**, extrapolation of the $\chi'_M T$ data from above 8 K to 0 K gives ~3.6 and ~5.3 cm^3 K mol^{-1}, respectively, consistent with the values expected for two independent $S = 3/2$ and $S = 2$ units (spin-only values 3.75 and 6.00 cm^3 K mol^{-1}, respectively). No χ''_M signals were observed, and thus **3** and **4** are not SMMs. The out-of-phase χ''_M signals of complexes **5** and **6** are tails of peaks lying below 1.8 K, suggesting **5** and **6** might be tetramers of Mn_3 SMMs.

High-frequency electron paramagnetic resonance (HF-EPR) studies. In order to more precisely determine the spin-Hamiltonian parameters of **5**, HF-EPR data were collected for a finely ground sample of **5**·$x$$CH_2Cl_2$ that was incorporated into a KBr pellet in order to avoid field-alignment of the micro-crystallites within the powder. Measurements were performed at multiple high frequencies in the 52.4 to 422.4 GHz range, and at temperatures from 3.5 to 20 K.

Temperature dependent EPR spectra collected at 217.6 GHz are presented in Fig. 9. The two very sharp features (indicated by asterisks) at 3.2 and 5.5 T have been well characterized and are attributed to paramagnetic oxygen impurities trapped in the KBr pellet. The sharp feature observed around the isotropic $g = 2.00$ position (marked by "×" at 7.77 T) corresponds to an impurity phase within the powder, possibly containing Mn^{II}; this is often found to be the case in Mn-containing polynuclear clusters. The spectra were recorded in field-derivative mode (dI/dB, where I denotes the absorption intensity), making it relatively easy to determine which peaks correspond to which components of the spectrum. The inset to Fig. 9a displays

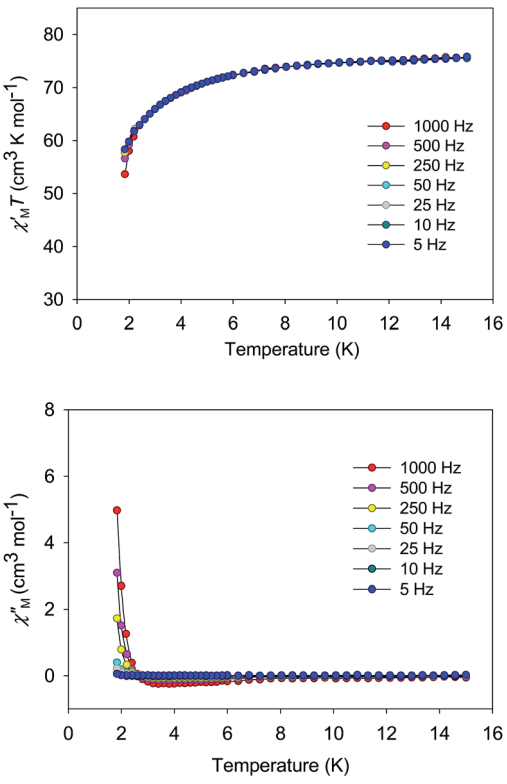

Fig. 8 Plot of the in-phase (χ'_M, as $\chi'_M T$) and out-of-phase (χ''_M) ac susceptibility data *vs.* T for **5**·$2CH_2Cl_2$ in a 3.5 G field oscillating at the indicated frequencies.

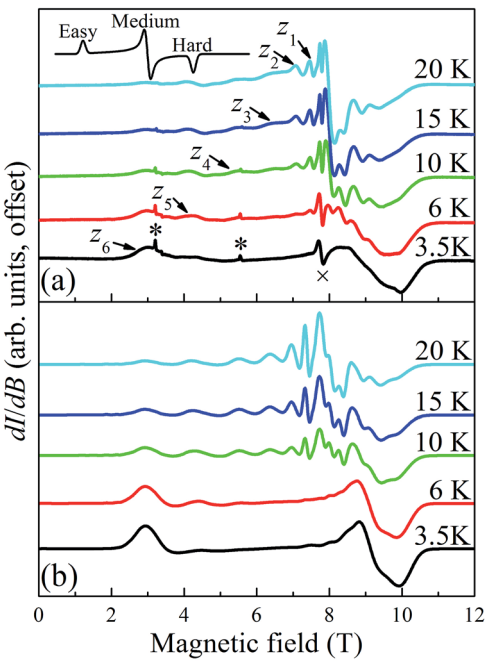

Fig. 9 Temperature dependence of HF-EPR spectra collected on a microcrystalline sample of complex **5**·$x$$CH_2Cl_2$ (experimental (a) and simulated (b)) restrained in KBr; the spectra were recorded in field derivative mode at 217.6 GHz in the 3.5 to 20 K range. The features in (a) are labeled according to the scheme described in the main text. The top inset in (a) depicts a typical derivative mode powder spectrum for a biaxial system, illustrating the features expected for the x-, y-, and z-components of the spectrum. The features in (a) marked by * and × are attributed to known impurities.

a trivial example of a $T = 0$ derivative mode powder spectrum for a biaxial $S = 1/2$ system with three distinct $\boldsymbol{g}$-tensor components: the onset of absorption appears as a peak in the derivative mode spectrum, and corresponds to the easy-axis of magnetization (largest $\boldsymbol{g}$ component); the cessation of absorption thus appears as a dip in the derivative, corresponding to the hard-axis (smallest $\boldsymbol{g}$ component); meanwhile, the intermediate component of the $\boldsymbol{g}$-tensor occurs at the maximum in absorption and, therefore, looks like the derivative of the z-component. The same general behavior is expected for high-spin systems that experience zero-field splitting (zfs) interactions, and examination of the resonances on the low (high) field side of $\boldsymbol{g} = 2.00$ in Fig. 9a indicates that they are indeed peaks (dips). In the case of a uniaxial zfs tensor, the parallel ($B\|z$) component of the powder spectrum typically extends about twice as far from the $\boldsymbol{g} = 2.00$ position, compared to the perpendicular ($B\perp z$) component, with the extent of the deviation from $\boldsymbol{g} = 2.00$ being directly proportional to the magnitude of the axial D parameter. On this basis, the multiple low-field features in Fig. 9a can be attributed to resolved parallel ($B\|z$) excitations. Careful inspection of the 20 K spectrum reveals six such peaks (z_1 to z_6) on the low field side of $\boldsymbol{g} = 2.00$. This is an indication of an $S = 6$ ground state for the Mn_3 triangle units. The peaks correspond to the following fine-structure transitions within the ground $S = 6$ spin multiplet: $m_S = -6 \rightarrow -5$ (z_6), $m_S = -5 \rightarrow -4$ (z_5), …, and $m_S = -1 \rightarrow 0$ (z_1). The fact that the spectral weight associated with the parallel spectrum shifts to the low field, $m_S = -6 \rightarrow -5$ (z_6), transition upon cooling provides confirmation of the negative sign of D, *i.e.*, the $m_S = -6$ state is lowest in energy when $B\|z$.

In contrast to the parallel spectrum, the fine structure transitions within the perpendicular spectrum are not resolved. There are several possible reasons for this. First of all, the relevant peaks should be much more closely spaced (two perpendicular components, each with half the separation of the parallel spectrum) and, therefore, more difficult to resolve. Nevertheless, this alone cannot account for the observed spectrum. Another compounding factor is the existence of the two distinct isosceles triangles (with short/short/long and long/long/short edges) within the tetramer (*vide supra*), which one would expect to have different zfs parameters, with the difference likely being more pronounced for the transverse 2nd-order anisotropy parameter, E. The transverse anisotropy results from a projection of the anisotropies of the individual Mn^{III} ions onto the plane of the triangle. The 2nd-order projection is strictly zero ($E = 0$) for the perfectly equilateral case, *i.e.*, there is an exact cancelation. However, for the isosceles case, the projections onto the plane of the triangle do not cancel, and the value of E can be expected to be extremely sensitive to the distortion away from a perfect equilateral triangle. This contrasts the case for the axial molecular zfs parameter, D, which results from an addition of the single-ion anisotropies. The effect of the two triangular topologies is therefore likely to be quite similar to a disorder that disproportionately affects the transverse anisotropy parameter, E. This type of disorder is well known in other Mn^{III} containing clusters,[105] including the Mn_{12}-acetate SMM,[106,107] where it has been shown to significantly impact the perpendicular spectrum without affecting the parallel components significantly. These influences can be taken into consideration when simulating spectra using a program such as EasySpin.[108] We note that the temperature dependent studies (Fig. 9) do not provide any strong indications that there are low-lying states with $S = 5$, 4, *etc.*, *i.e.*, no additional peaks emerge upon raising the temperature that cannot be accounted for *via* simulations that assume an isolated $S = 6$ ground state.

Fig. 9b displays the simulation obtained from the spin Hamiltonian in eqn (9), where $\hat{S}$ and $\hat{S}_i$ ($i = x, y, z$) are spin operators,

$$\hat{H} = \mu_B \vec{B}\cdot\boldsymbol{g}\cdot\hat{S} + D\hat{S}_z^{\,2} + E\left(\hat{S}_x^{\,2} - \hat{S}_y^{\,2}\right) + B_4^0\hat{O}_4^0 \qquad (9)$$

$\vec{B}$ is the applied magnetic field vector, $\overleftrightarrow{\boldsymbol{g}}$ is the Landé $\boldsymbol{g}$ tensor, D and E are the second-order axial and rhombic zfs parameters, respectively, and the final term represents an axial fourth-order zfs interaction.[108] The parameters used for the simulation are $S = 6$, $D = -0.33$ cm^{-1}, $|E| = 0.030$ cm^{-1}, $B_4^0 = -8.0 \times 10^{-5}$ cm^{-1}, and $\boldsymbol{g}_x = \boldsymbol{g}_y = \boldsymbol{g}_z = 2.00$. As can be seen, the relevant parallel and perpendicular portions of the simulations agree with the experiments very well, and the obtained D value is consistent with that deduced from the magnetic studies. Gaussian distributions of the D and E parameters ($\sigma_D = 8\%$, $\sigma_E = 40\%$) were employed in order to reproduce the observed line broadening. As expected, the strain in E is much more pronounced than that of D, which explains the almost complete loss of resolution of the transverse part of the EPR spectrum.

In order to obtain tighter constraints on the spin Hamiltonian parameters for complex $\mathbf{5}\cdot x CH_2Cl_2$, the positions of parallel component peaks obtained at multiple frequencies are displayed on a 2D frequency *vs.* field plot in Fig. 10. The combined data set was then simulated using the Hamiltonian of eqn (9); the solid lines in Fig. 10 represent the best simulation using the same parameters as those used in Fig. 9b. We note that the fourth-order $B_4^0\hat{O}_4^0$ term is absolutely essential to the

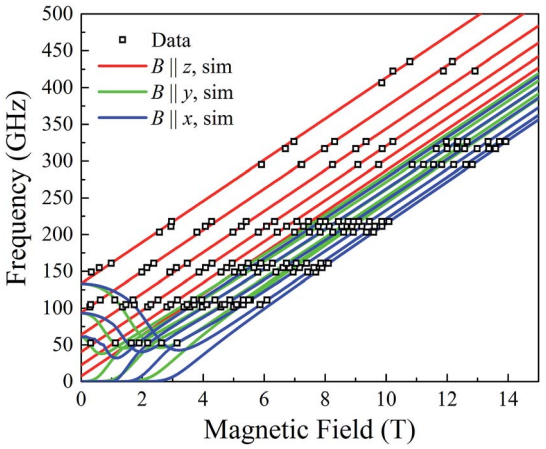

Fig. 10 2-D plot of frequency *vs.* the field locations of powder EPR spectral features observed for $\mathbf{5}\cdot x CH_2Cl_2$ at multiple frequencies in the 52.4 to 422.4 GHz range. Simulated transition curves employing eqn (9) are included for $B\|x$ (blue), y (green) and z (red). See the text for the simulation parameters.

simulations, accounting for the uneven field spacing of the resonances. One can estimate a kinetic barrier (U) to magnetization relaxation of ~12 cm^{-1} from the S and D values or ~15 cm^{-1} if the effect of the significant B_4^0 is included.

We conclude this section by discussing the interaction between the four Mn_3 units in the tetramer. EPR spectra for the powder sample suggest that the Mn_3 units are essentially uncoupled, or the coupling is too weak to detect by EPR. Hysteresis loop data suggest an antiferromagnetic coupling of -0.0076 cm^{-1} (*vide infra*) between adjacent Mn_3 units within the tetramer. This coupling is smaller than the D and E strains ($\sigma_D = 0.026$ cm^{-1} and $\sigma_E = 0.012$ cm^{-1}), which means that the spectral broadening (FWHM $= 2.35\sigma$) is likely to far exceed any additional splittings of the EPR spectra induced by the inter-SMM exchange. Consequently, it cannot be detected by EPR.

The picture that emerges from the combined magnetic and HF-EPR studies on **5** and **6** described above is that magnetically-supramolecular aggregates of the Mn_3 SMMs with $S = 6$ can be obtained using the dioximate $pdpd^{2-}$, and that these do indeed contain Mn_3 units that still retain the structural and magnetic properties of the monomeric analogue **2**. Any inter-Mn_3 exchange interactions through the dioximate groups are either zero or too weak to affect the magnetic data collected above 1.8 K. The tetramers **5** and **6** therefore behave as an assembly of independent Mn_3 units and their data can be fit as such to give fit parameters that are essentially identical with those previously obtained for **2**. The crucial question now needing to be addressed is whether there are indeed any inter-Mn_3 interactions present, and if so what is their effect? The answers to these questions required studies at even lower temperatures.

Magnetization hysteresis and decay studies. Magnetization (M) *vs.* dc field scans on a single crystal of **5**·$x$$CH_2Cl_2$ were carried out on a micro-SQUID using field sweep rates in the 0.001–0.280 T s^{-1} range.[78] Hysteresis loops were observed below ~1.0 K (Fig. 11) whose coercivities increase with decreasing temperature and increasing field sweep rate, as expected for SMMs. The loops also exhibit a number of steps characteristic of quantum tunnelling of magnetization (QTM). The blocking temperature is ~1.0 K, above which M relaxes faster than the time scale of the hysteresis measurement. We therefore conclude that each of the four Mn_3 units in **5**·$x$$CH_2Cl_2$ is an SMM, as previously found for monomer **2**, which they closely resemble.

Before analysing the QTM step pattern, we describe the determination of the effective relaxation barrier (U_{eff}) from magnetization decay measurements. A large dc magnetic field was applied to the crystal at ~5 K to saturate the magnetization in one direction, and T decreased to a chosen value in the 0.03–1.0 K range. The field was then removed and M measured as a function of time (Fig. 12, inset). From these data, relaxation time (τ) *vs.* T data were extracted and used to construct an Arrhenius plot based on eqn (10) (Fig. 12), where k is the Boltzmann constant. Below ~0.3 K, τ is temperature-independent

$$\ln(\tau) = \ln(\tau_0) + U_{eff}/kT \quad (10)$$

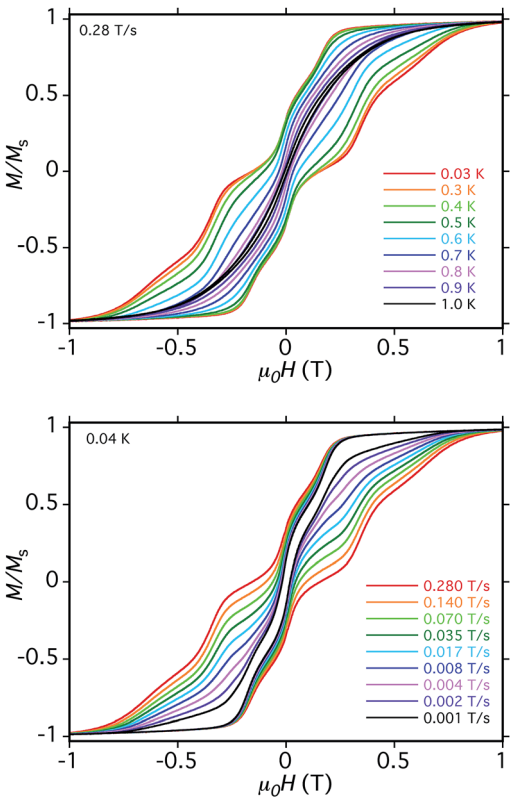

Fig. 11 Magnetization *vs.* dc field hysteresis loops for a single crystal of **5**·$x$$CH_2Cl_2$ at the indicated temperatures (top) and field scan rates at 0.04 K (bottom). M is normalized to its saturation value, M_S.

and all relaxation is by QTM *via* the lowest energy $m_S = \pm 6$ levels of the ground state $S = 6$ manifold. Above ~0.3 K, the relaxation is thermally activated, and a fit of the linear region at higher T (dashed line in Fig. 12) gave $U_{eff} = 8.5$ cm^{-1} ($U_{eff}/k_B = 12.2$ K) and $\tau_0 = 5 \times 10^{-9}$ s. The U_{eff} is smaller than the upper limit to the barrier ($U = S^2|D| \sim 11.9$ cm^{-1} ($U/k_B = 17.1$ K)) calculated using D from the EPR data. This is as expected for QTM *via*

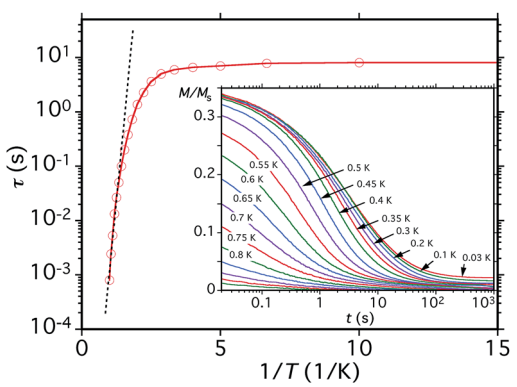

Fig. 12 Relaxation time (τ) *vs.* $1/T$ plot for a single crystal of **5**·$x$$CH_2Cl_2$ obtained from the dc magnetization decay *vs.* time data in zero applied field at the indicated temperatures. The dashed line is the fit of the thermally-activated region to the Arrhenius equation. See the text for the fit parameters.

a thermally (phonon) assisted pathway involving higher-energy m_S levels of the $S = 6$ ground state.

We now address whether the four Mn_3 SMM units in $\mathbf{5}\cdot x CH_2Cl_2$ are weakly interacting with each other. The answer is clearly yes because the hysteresis loops show an exchange-bias (shift) of the QTM steps. The first step in the hysteresis loop of an SMM on scanning from negative to positive fields is normally at zero field, where the m_S levels on either side of the anisotropy barrier are in resonance and QTM can occur, reversing the orientation of the magnetization vector. The presence of an AF exchange-coupled neighbor provides a bias field that shifts the QTM step (resonance tunneling) to a new field position before zero. This was first seen for the hydrogen-bonded $[Mn_4]_2$ dimer of $S = 9/2$ SMMs,[26] and a related explanation is valid for **5**, except that each Mn_3 SMM will be seen to be exchange-coupled to two neighboring Mn_3 SMMs *via* the bridging $pdpd^{2-}$ groups.

The loops for $\mathbf{5}\cdot x CH_2Cl_2$ in Fig. 11 show the first QTM step before zero field, confirming weak AF interactions between the Mn_3 subunits. However, there is still a step at zero field and at a slow sweep rate of 0.001 T s^{-1}, a third step is evident after zero field giving a three-step pattern with equal step separations that is symmetric about zero field. This is unlike anything seen previously in exchange-biased dimers. At faster sweep rates, the step patterns change markedly, the symmetric three-step pattern being lost and new steps appearing. The overall loop profiles and their sweep-rate dependence point to a more complicated exchange-coupled system than any encountered previously and which needed to be carefully explained.

To obtain a simplified spin Hamiltonian to model the $[Mn_3]_4$ tetramer, each Mn_3 SMM can be treated as a giant spin of $S = 6$ with easy-axis anisotropy. The spin Hamiltonian ($\hat{H}$) for each Mn_3 is given by eqn (11), where $i = 1$–4 refers to the four Mn_3 SMMs of the tetramer (Fig. 13), μ_0 is the vacuum permeability,

$$\hat{H}_i = D\hat{S}_{z,i}{}^2 + \hat{H}_{\mathrm{trans},i} + \boldsymbol{g}\mu_B\mu_0\hat{S}_{zi}\cdot H_z \quad (11)$$

and H_z is the applied longitudinal field.[26] The last term is the Zeeman energy associated with the applied field. The exact form of the transverse anisotropy $\hat{H}_{\mathrm{trans},i}$ is not important in this discussion. The general Hamiltonian for the tetramer is then given by eqn (12), where J_{ij} are exchange coupling parameters between

$$\hat{H} = \sum\hat{H}_i - \sum 2J_{ij}\hat{S}_i\cdot\hat{S}_j \quad (12)$$

subunits i and j, $S_i = S_j = 6$, and the exchange interactions are assumed to be isotropic ($J_z = J_{xy}$).

Since **5** is a rectangular $[Mn_3]_4$ aggregate, and assuming the interactions are superexchange couplings through the $pdpd^{2-}$ linkers (this assumption will be confirmed later), there should be two different inter-Mn_3 interactions, J_1 and J_2, which are likely to be comparable but not identical in magnitude; the diagonal interaction (J_{13}) should be essentially zero and can be ignored. Therefore, the spin Hamiltonian is given in eqn (13).

$$\hat{H} = \hat{H}_1 + \hat{H}_2 + \hat{H}_3 + \hat{H}_4 - 2J_1(\hat{S}_1\cdot\hat{S}_2 + \hat{S}_3\cdot\hat{S}_4) - 2J_2(\hat{S}_1\cdot\hat{S}_4 + \hat{S}_2\cdot\hat{S}_3) \quad (13)$$

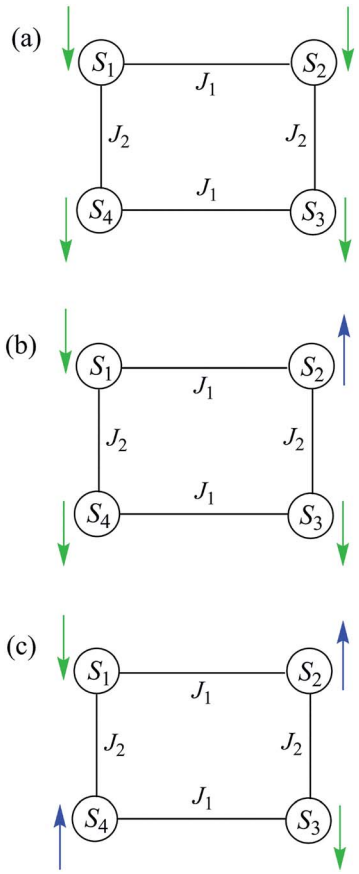

Fig. 13 Labelling scheme used in the spin Hamiltonians of eqn (11)–(15), and the QTM transitions described in the text.

Tunnelling among the $(2S + 1)^4 = 28\,561$ energy states is allowed by the small transverse anisotropy $\hat{H}_{\mathrm{trans},i}$ and the transverse coupling terms containing $\hat{S}_{xi}$ and $\hat{S}_{yi}$ operators. Calculating the energy states of $[Mn_3]_4$ by exact diagonalization would be a major undertaking, and for convenience we instead neglect all transverse anisotropy terms. The spin Hamiltonian in eqn (13) can then be rewritten as eqn (14).

$$\hat{H} \approx \hat{H}_1 + \hat{H}_2 + \hat{H}_3 + \hat{H}_4 - 2J_1(\hat{S}_{1z}\hat{S}_{2z} + \hat{S}_{3z}\hat{S}_{4z}) - 2J_2(\hat{S}_{1z}\hat{S}_{4z} + \hat{S}_{2z}\hat{S}_{3z}) \quad (14)$$

Since $J_1 \approx J_2$, we shall assume for now that $J_1 = J_2 = J$. The eigenvalues of eqn (14) are then given by eqn (15).

$$E = D(m_{S1}{}^2 + m_{S2}{}^2 + m_{S3}{}^2 + m_{S4}{}^2) + \boldsymbol{g}\mu_B\mu_0 H_z(m_{S1} + m_{S2} + m_{S3} + m_{S4}) - 2J(m_{S1}m_{S2} + m_{S3}m_{S4} + m_{S1}m_{S4} + m_{S2}m_{S3}) \quad (15)$$

The hysteresis loops at 0.04 K as a function of sweep rate (Fig. 11, bottom) can now be explained, and we shall do so in two parts: (i) the origin of the symmetric three-step loop at 0.001 T s^{-1}, and (ii) the changes that occur at higher sweep rates. As a preliminary, the consideration of the step pattern expected for AF coupling of a Mn_3 unit with one, two or three neighboring Mn_3 units led to the conclusion that the observed symmetric three-step pattern with the central one at zero field can only result from coupling to two neighbors, consistent with the

rectangular topology of **5**. Coupling to one or three neighbors should exhibit no steps at zero field since there will always be a net bias present from the odd number of neighbors; only for two neighbors can the net bias be zero – namely, in the case when their two effects cancel out, as will be described below.

The spin-state energy *vs.* applied dc field was calculated using eqn (15) for all the states of **5**. It was then adjusted by varying the magnitude of J and D to simulate the experimental hysteresis loop at 0.001 T s^{-1}. The resulting plot (Fig. 14, top) was obtained with $J = -0.0076$ cm^{-1} ($J/k_B = -0.011$ K) ($\hat{H} = -2J\hat{S}_i\cdot\hat{S}_j$ convention) and $D = -0.33$ cm^{-1}. When the spin Hamiltonian contains transverse terms ($\hat{H}_{trans}$), the level crossings can be 'avoided level crossings'. The spin S is "in resonance" between two states when the local longitudinal field is close to an avoided level crossing, and tunneling may occur. The plot shows all avoided level crossings at which QTM transitions could be seen, and we can now explain the three-step hysteresis loop at 0.001 T s^{-1} in Fig. 11, bottom.

At the lowest T of 0.04 K, only the lowest energy states involving $m_S = \pm 6$ states will be populated (red lines in Fig. 14). As the field is scanned from −1 T, where the four Mn_3 magnetization vectors will have all been polarized into the $m_S = -6$ orientation (Fig. 13a), the following is seen:

(a) the first QTM step corresponds to tunneling of a Mn_3 vector from the $m_S = -6$ to the $m_S = +6$ state; this occurs at −0.19 T, which thus represents the total bias field from two $m_S = -6$ neighbours. In the format (m_{S1}, m_{S2}, m_{S3}, m_{S4}), where i = 1–4 are the four Mn_3 SMMs within **5**, the −0.19 T step corresponds to the (−6, −6, −6, −6) to (−6, +6, −6, −6) tunneling transition (Fig. 13b); for convenience, other possible equivalent product states, (+6, −6, −6, −6), (−6, −6, +6, −6), and (−6, −6, −6, +6), are not shown;

(b) the second step at zero field is assigned to tunneling of molecules with −6, +6 neighbors (S_1 and S_3 in Fig. 13b), which therefore experience a zero bias (if $J_1 = J_2$, or a small bias related to $|J_1 - J_2|$ if $J_1 \neq J_2$). The step at zero field is thus the (−6, +6, −6, −6) to (−6, +6, +6, −6) tunneling transition, which will then have some probability of undergoing a spin flip-flop relaxation to the (−6, +6, −6, +6) ground state since J is AF (Fig. 13c);

(c) If enough vectors have tunnelled in the first two steps to +6 (*i.e.*, if the sweep rate is slow enough), then a third step is expected for Mn_3 vectors tunneling in the presence of a +6, +6 bias field (S_1 and S_3 in Fig. 13c). This would be symmetrically located with respect to the first step, and should thus occur at +0.19 T.

The three-step pattern at 0.001 T s^{-1} sweep rate (in Fig. 11, bottom) is thus as predicted at this slow scan rate, which is required to see situation (c). Note that the avoided level crossings at positions marked with asterisks might at first glance be predicted to give additional QTM steps, but these involve multiple (2, 3, or 4) tunneling transitions at the same time, *e.g.* (−6, −6, −6, −6) to (−6, +6, +6, −6), (−6, −6, −6, −6) to (−6, +6, +6, +6), *etc.* They thus have a very low probability of occurring and in fact we see no evidence for their occurrence. Note that double tunneling transitions also occur at ±0.19 T and 0 T, *i.e.*, at the avoided level crossings where the single transitions are seen as steps in the loops.

At faster scan rates, the three-step hysteresis loop changes markedly. On scanning from −1 T at 0.28 T s^{-1}, the first step has now decreased in size, as has the second step at zero field, and the third step has disappeared completely. This is as expected from standard Landau–Zener theory,[109,110] which predicts that the tunneling probability decreases with increasing field scan rate, *i.e.* fewer molecules are in resonance long enough for their spins to tunnel. As these steps decrease or disappear, new steps appear in the 0.0–1.0 T range as the magnetization relaxes *via* alternative tunnelling pathways; some steps appear and disappear as the scan rate increases (*e.g.* at 0.35 T), and by 0.28 T s^{-1} two broad features at ~0.4 T and ~0.6 T are evident. We assign these tunneling transitions to levels involving one $m_S = \pm 5$ state, *i.e.*, at positions involving avoided level crossings of red and blue lines in Fig. 14. These include (−6, −6, −6, −6) to (−6, +6, −6, −5) at ~0.1 T, (−6, +6, −6, −6) to (−6, +6, +6, −5) at ~0.2 T, (−6, +6, −6, −6) to (−6, +6, +6, −5) at ~0.4 T, (−6, +6, −6, +6) to (−6, +6, +5, +6) at ~0.6 T, and others.

It should be noted that all the steps in Fig. 11 are rather broad compared with, *e.g.*, those for monomer **2** (Fig. S14†).

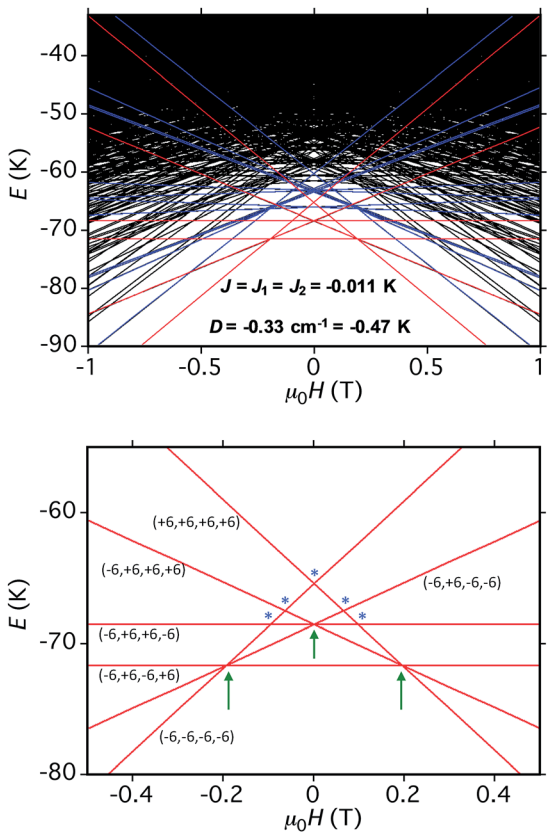

Fig. 14 (Top) simulation with $J = -0.0076$ cm^{-1} ($J/k_B = -0.011$ K), ($\hat{H} = -2J\hat{S}_i\cdot\hat{S}_j$ convention) and $D = -0.33$ cm^{-1} of the spin state energies *vs.* applied dc field for an $[Mn_3]_4$ tetramer of $S = 6$ SMMs using eqn (15): red = spin states involving only the $m_S = \pm 6$ states of the four Mn_3 sub-units; blue = spin states involving both $m_S = \pm 6$ states and one $m_S = \pm 5$ state; black = other states. (Bottom) spin states involving only the $m_S = \pm 6$ states and their identity. * = multiple spin flips (2, 3 or 4) at the same time. The green arrows are the avoided level crossings at which QTM leads to the three steps at 0.001 T s^{-1} in Fig. 11.

This is due to the two independent cations in the asymmetric unit having different orientations, and the four Mn_3 planes within each cation not being coplanar (Fig. 4, bottom). As a result, the applied field will be at a range of angles to the *z*-axes (easy-axes) of the eight Mn_3, leading to step broadening. This is unfortunate because had the steps been sharper, we might have been able to resolve the different tunneling transitions that occur at different sweep rates in the hysteresis loops. We did attempt to collect micro-SQUID data on single crystals of $\mathbf{6}\cdot x CH_2Cl_2$ but they were more fragile than those of $\mathbf{5}\cdot x CH_2Cl_2$ and we could not get satisfactory data.

As a further test of the validity of the above model and Fig. 14, we carried out hysteresis minor-loop sweeps from −1 T to various fields up to zero and then reversed the sweep direction. The objective was to scan through the avoided level crossing centered at −0.19 T to allow some molecules to tunnel from (−6, −6, −6, −6) to (−6, +6, −6, −6), *i.e.*, step (a) above, and then on reversing the sweep to see the (−6, +6, −6, −6) to (−6, −5, −6, −6) QTM transition at just under −0.55 T (Fig. 15, inset). The separation between these two QTM steps is proportional to the energy difference between the (−6, −6, −6, −6) and (−6, −5, −6, −6) states, *i.e.*, it depends on *D*. The desired step was observed, although broad due to the factors discussed above. Nevertheless, a field separation of $\Delta H \approx 0.4$ T could be estimated. Using eqn (16) gives $D \approx -0.37$ cm^{-1} with $g = 2.0$, in satisfying agreement with values obtained from the magnetization and HF-EPR fits, and thus supporting the overall validity of the model and the analysis of the hysteresis loops. The value of *D* suggests the population of Mn_3 units sampled in the minor-loop scans had an average angle between their *z*-axes and the applied field of ∼28°.

$$|D| = g\mu_B \Delta H \quad (16)$$

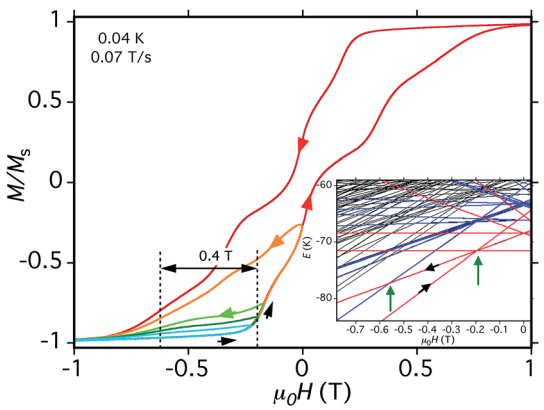

Fig. 15 Hysteresis loop and minor loops at the indicated *T* and sweep rate. The field was swept from −1.0 T and then reversed at various field positions to probe the separation of the (−6, +6, −6, −6) to (−6, −5, −6, −6) QTM step from the (−6, −6, −6, −6) to (−6, +6, −6, −6) step, which depends on *D*. The different colors are to distinguish different sweeps. (Inset) portion of the spin state energy plot of Fig. 14, showing with green arrows the two avoided level crossings and associated QTM transitions being probed.

Validity of assumptions. The above discussion explains the sweep rate dependence of the hysteresis loops for $\mathbf{5}\cdot x CH_2Cl_2$, and the general conclusion reached is that each Mn_3 SMM is interacting with its two neighbors in the rectangle to which it is linked by the bridging pdpd^{2-} linkers. We now address two important follow-up questions: (i) is it safe to assume that the two neighbors with which each Mn_3 is interacting are those connected to it by the pdpd^{2-} linkers? And (ii) is the assumption that $J_1 = J_2$ valid, and how would we know if it is not?

It could be argued that the pdpd^{2-} linkers are not the superexchange pathways through which the Mn_3 interact. Might the interactions instead be dipolar between a Mn_3 and nearby neighbors (intra- or inter-tetramer), or *via* inter-tetramer π-stacking or weak H-bonds? However, $\mathbf{5}\cdot x CH_2Cl_2$ contains no significant inter-tetramer contacts, other than some C–H···π and π···π contacts involving the central Ph ring of the pdpd^{2-} group, and many C–H···Cl H-bonds to the solvent molecules. Nevertheless, we compared inter-tetramer distances and contacts in $\mathbf{5}\cdot x CH_2Cl_2$ crystals with those in $\mathbf{2}\cdot 3CH_2Cl_2$. Shortest inter-$Mn_3$ Mn···Mn distances are comparable (Fig. S4†), ∼6.0 and ∼6.6 Å in **5** and **2**, respectively, and similar C–H···π, π···π, and C–H···Cl contacts are present in both. In fact, **2** contains π···π stacking between the pyridyl rings on neighboring Mn_3 units (**5** does not) and thus might be expected to give stronger inter-Mn_3 exchange couplings than in **5**. Thus, if the inter-Mn_3 couplings that give the exchange-biased QTM in **5** were dipolar in origin or superexchange through any of the mentioned contacts, we would expect to see similar (or even larger) shifts of the QTM steps in **2**. In fact, the hysteresis loops of $\mathbf{2}\cdot 3CH_2Cl_2$ show no discernible shift of the zero field step (Fig. S14†). We thus conclude that the only significant inter-Mn_3 coupling leading to the exchange-biased QTM in $\mathbf{5}\cdot x CH_2Cl_2$ is indeed superexchange through the pdpd^{2-} linkers.

The rectangular structure of **5** suggests $J_1 \neq J_2$, although both should be very weak. We therefore calculated what might be expected in this case, and whether we might be able to identify this difference experimentally. A representative energy plot calculated with a reasonable $J_1/J_2 = 0.7$ ratio is shown in Fig. S15,† where it is also compared with the $J_1 = J_2$ plot. The only change to the three-step hysteresis loop of the $J_1 = J_2$ situation is the step at zero-field splitting into two, with splitting proportional to $|J_1 - J_2|$. The other steps still occur symmetrically about zero at $\pm(J_1 + J_2)$. With better step resolution, we might have been able to pick up a splitting in the zero-field peak, but the broadness of the steps due to the range of magnetic field alignments, as described above, precludes this. We thus conclude that even though it is likely that $J_1 \neq J_2$, the difference must be too small to have a noticeable effect on the hysteresis loops within the experimental step broadness.

Conclusions

We summarize below the main results and conclusions of this study:

(1) Employment of a designed dioxime group has allowed the isolation from straightforward procedures of two non-SMM $[Mn_3]_2$ and two SMM $[Mn_3]_4$ aggregates; the latter serve to

achieve the overall objective of this work, to obtain covalently-linked oligomers of SMMs to extend previous work beyond the dimeric systems studied in the past. The dioxime was not pre-programmed to give any particular oligomer topology, and a rectangular one was obtained.

(2) Each Mn_3 SMM subunit in $[Mn_3]_4$ tetramers has retained the structure and magnetic properties of the monomeric analogue, encouraging us that the oligomerization methodology has the potential for general application to a range of linkers without damage to the units or their SMM properties.

(3) Carboxylate substitution on preformed $[Mn_3]_4$ tetramer **5** has been accomplished without rupture of the oligomer linkages, providing a convenient means for post-synthetic modification of oligomers for comparative studies or certain applications.

(4) Lower dioxime : Mn ratios afford $[Mn_3]_2$ dimers at two oxidation levels, $[Mn^{II}Mn^{III}_2]_2$ and $[Mn^{III}_3]_2$, with asymmetric ligation not previously observed, leading to a mix of F and AF exchange interactions in both complexes.

(5) The magnetic analysis confirms that each Mn_3 unit is still ferromagnetically-coupled with an $S = 6$ ground state, and there is no evidence in the data at 1.8 K and above for any inter-Mn_3 exchange-interactions. In addition, both types of distortion of the Mn_3 triangles from equilateral to isosceles have been seen and magnetically analyzed, characterizing two best-fit minima in the error surface and the degree of difference caused to the constituent J values.

(6) Detailed multi-frequency HF-EPR spectra at a range of temperatures, and their simulations, have provided the important spin Hamiltonian parameters to fourth order, confirming that the oligomerization has minimal effect on the intra-Mn_3 magnetic properties, and addressing the difficulty of detecting by HF-EPR very weak inter-Mn_3 interactions.

(7) Hysteresis loops obtained on a single crystal of $\mathbf{5}\cdot x CH_2Cl_2$ established that the four Mn_3 SMMs are each weakly coupled to two neighbors, and this interaction is manifested as an exchange-bias of the QTM steps, with the exact positions of the latter determined by the spin alignments at these two neighbors. The exchange-biased hysteresis loops at 0.04 K and 0.001 T s^{-1} scan rates have been explained by identification of the ground state quantum transitions taking place.

(8) Equally important, the large changes in QTM step locations at higher scan rates have been explained as a function of decreasing tunneling probability with increasing scan rate, resulting in relaxation *via* QTM transitions involving higher energy levels.

(9) Using the hysteresis loop of the analogous Mn_3 monomer as a control, a crucial conclusion has been reached that the inter-Mn_3 interaction is *via* superexchange through the bridging dioximate linkers. This shows that intra-oligomer couplings and quantum effects can be studied in the solid state without complications from dipolar or other inter-oligomer pathways.

(10) The validity of the overall model used to describe the quantum behavior has been tested by simulations of the 1- or 2-J coupling model, and also by hysteresis minor-loop studies that have been shown to give a Mn_3 D value comparable to those from the magnetization fits and HF-EPR studies.

Overall, the described work represents a rational approach to obtaining covalently-connected multiple Mn_3 SMMs that is now being extended to other oligomers with various structural topologies and quantum mechanical couplings in order to assess their potential for use as multi-qubit assemblies and other systems based on SMMs.

Acknowledgements

This work was supported by the USA National Science Foundation (GC: CHE-0910472, DMR-1213030; SH: DMR-1309463) and by the Air Force (SH: AOARD grant #134031). WW acknowledges grants FP7-ICT-2013-10-610449 MoQuaS and ANR-13-BS10-0001-03 MolQuSpin. T. N. N thanks the Vietnam Education Foundation for a fellowship. Work performed at the NHMFL is supported by the USA National Science Foundation (DMR-1157490) and the State of Florida.

References

1 R. Sessoli, D. Gatteschi, A. Caneschi and M. A. Novak, *Nature*, 1993, **365**, 141–143.
2 R. Sessoli, H. L. Tsai, A. R. Schake, S. Wang, J. B. Vincent, K. Folting, D. Gatteschi, G. Christou and D. N. Hendrickson, *J. Am. Chem. Soc.*, 1993, **115**, 1804–1816.
3 G. Christou, D. Gatteschi, D. N. Hendrickson and R. Sessoli, *MRS Bull.*, 2000, **25**, 66–71.
4 G. Christou, *Polyhedron*, 2005, **24**, 2065–2075.
5 R. Bagai and G. Christou, *Chem. Soc. Rev.*, 2009, **38**, 1011–1026.
6 V. I. Ovcharenko and R. Z. Sagdeev, *Russ. Chem. Rev.*, 1999, **68**, 345–363.
7 J. S. Miller and A. J. Epstein, *MRS Bull.*, 2000, **25**, 21–30.
8 S. J. Blundell and F. L. Pratt, *J. Phys.: Condens. Matter*, 2004, **16**, R771–R828.
9 J. S. Miller, *Chem. Soc. Rev.*, 2011, **40**, 3266–3296.
10 A. J. Tasiopoulos, A. Vinslava, W. Wernsdorfer, K. A. Abboud and G. Christou, *Angew. Chem., Int. Ed.*, 2004, **43**, 2117–2121.
11 J. R. Friedman, M. P. Sarachik, J. Tejada and R. Ziolo, *Phys. Rev. Lett.*, 1996, **76**, 3830–3833.
12 L. Thomas, L. Lionti, R. Ballou, D. Gatteschi, R. Sessoli and B. Barbara, *Nature*, 1996, **383**, 145–147.
13 W. Wernsdorfer and R. Sessoli, *Science*, 1999, **284**, 133–135.
14 W. Wernsdorfer, M. Soler, G. Christou and D. N. Hendrickson, *J. Appl. Phys.*, 2002, **91**, 7164–7166.
15 W. Wernsdorfer, N. E. Chakov and G. Christou, *Phys. Rev. Lett.*, 2005, **95**, 037203.
16 W. Wernsdorfer, S. Bhaduri, R. Tiron, D. N. Hendrickson and G. Christou, *Phys. Rev. Lett.*, 2002, **89**, 197201.
17 S. Hill, R. S. Edwards, N. Aliaga-Alcalde and G. Christou, *Science*, 2003, **302**, 1015–1018.
18 A. Wilson, S. Hill, R. S. Edwards, N. Aliaga-Alcalde and G. Christou, *AIP Conf. Proc.*, 2006, **850**, 1141–1142.
19 R. Tiron, W. Wernsdorfer, D. Foguet-Albiol, N. Aliaga-Alcalde and G. Christou, *Phys. Rev. Lett.*, 2003, **91**, 227203.
20 M. N. Leuenberger and D. Loss, *Nature*, 2001, **410**, 789–793.

21 B. Zhou, R. Tao, S.-Q. Shen and J.-Q. Liang, *Phys. Rev. A*, 2002, **66**, 010301.
22 M. Affronte, F. Troiani, A. Ghirri, A. Candini, M. Evangelisti, V. Corradini, S. Carretta, P. Santini, G. Amoretti, F. Tuna, G. Timco and R. E. P. Winpenny, *J. Phys. D: Appl. Phys.*, 2007, **40**, 2999–3004.
23 R. Vincent, S. Klyatskaya, M. Ruben, W. Wernsdorfer and F. Balestro, *Nature*, 2012, **488**, 357–360.
24 L. Bogani and W. Wernsdorfer, *Nat. Mater.*, 2008, **7**, 179–186.
25 K. Katoh, H. Isshiki, T. Komeda and M. Yamashita, *Chem.–Asian. J.*, 2012, **7**, 1154–1169.
26 W. Wernsdorfer, N. Aliaga-Alcalde, D. N. Hendrickson and G. Christou, *Nature*, 2002, **416**, 406–409.
27 R. Tiron, W. Wernsdorfer, N. Aliaga-Alcalde and G. Christou, *Phys. Rev. B: Condens. Matter Mater. Phys.*, 2003, **68**, 140407.
28 E.-C. Yang, W. Wernsdorfer, S. Hill, R. S. Edwards, M. Nakano, S. Maccagnano, L. N. Zakharov, A. L. Rheingold, G. Christou and D. N. Hendrickson, *Polyhedron*, 2003, **22**, 1727–1733.
29 L. M. Wittick, K. S. Murray, B. Moubaraki, S. R. Batten, L. Spiccia and K. J. Berry, *Dalton Trans.*, 2004, 1003–1011.
30 R. Bagai, W. Wernsdorfer, K. A. Abboud and G. Christou, *J. Am. Chem. Soc.*, 2007, **129**, 12918–12919.
31 R. Inglis, L. F. Jones, K. Mason, A. Collins, S. A. Moggach, S. Parsons, S. P. Perlepes, W. Wernsdorfer and E. K. Brechin, *Chem.–Eur. J.*, 2008, **14**, 9117–9121.
32 A. Das, K. Gieb, Y. Krupskaya, S. Demeshko, S. Dechert, R. Klingeler, V. Kataev, B. Buchner, P. Muller and F. Meyer, *J. Am. Chem. Soc.*, 2011, **133**, 3433–3443.
33 A. E. Thuijs, G. Christou and K. A. Abboud, *Acta Crystallogr., Sect. C: Struct. Chem.*, 2015, **71**, 185–187.
34 M. Murugesu, R. Clerac, W. Wernsdorfer, C. E. Anson and A. K. Powell, *Angew. Chem., Int. Ed.*, 2005, **44**, 6678–6682.
35 C. Coulon, H. Miyasaka and R. Clérac, *Struct. Bonding*, 2006, **122**, 163–206.
36 H. Miyasaka, K. Nakata, L. Lecren, C. Coulon, Y. Nakazawa, T. Fujisaki, K. Sugiura, M. Yamashita and R. Clérac, *J. Am. Chem. Soc.*, 2006, **128**, 3770–3783.
37 E. E. Moushi, T. C. Stamatatos, W. Wernsdorfer, V. Nastopoulos, G. Christou and A. J. Tasiopoulos, *Angew. Chem., Int. Ed.*, 2006, **45**, 7722–7725.
38 H. Miyasaka and M. Yamashita, *Dalton Trans.*, 2007, 399–406.
39 H.-B. Xu, B.-W. Wang, F. Pan, Z.-M. Wang and S. Gao, *Angew. Chem., Int. Ed.*, 2007, **46**, 7388–7392.
40 L. Bogani, A. Vindigni, R. Sessoli and D. Gatteschi, *J. Mater. Chem.*, 2008, **18**, 4750–4758.
41 O. Roubeau and R. Clérac, *Eur. J. Inorg. Chem.*, 2008, 4325–4342.
42 L. F. Jones, A. Prescimone, M. Evangelisti and E. K. Brechin, *Chem. Commun.*, 2009, 2023–2025.
43 S. K. Langley, N. F. Chilton, B. Moubaraki and K. S. Murray, *Dalton Trans.*, 2011, **40**, 12201–12209.
44 T. Shiga, H. Miyasaka, M. Yamashita, M. Morimoto and M. Irie, *Dalton Trans.*, 2011, **40**, 2275–2282.
45 G. Wu, J. Huang, L. Sun, J. Bai, G. Li, E. Cremades, E. Ruiz, R. Clérac and S. Qiu, *Inorg. Chem.*, 2011, **50**, 8580–8587.
46 I.-R. Jeon and R. Clérac, *Dalton Trans.*, 2012, **41**, 9569–9586.
47 Y. Liu, Z. Chen, J. Ren, X.-Q. Zhao, P. Cheng and B. Zhao, *Inorg. Chem.*, 2012, **51**, 7433–7435.
48 A. D. Katsenis, R. Inglis, A. Prescimone, E. K. Brechin and G. S. Papaefstathiou, *CrystEngComm*, 2012, **14**, 1216–1218.
49 D. Gatteschi and A. Vindigni, Single-Chain Magnets, in *Molecular Magnets-Physics and Applications*, ed. J. Bartolome, F. Luis and J. F. Fernandez, NanoScience and Technology Series, Springer, Verlag Berlin Heidelberg, 2014, pp. 191–220.
50 D. P. Giannopoulos, A. Thuijs, W. Wernsdorfer, M. Pilkington, G. Christou and T. C. Stamatatos, *Chem. Commun.*, 2014, **50**, 779–781.
51 The term 'magnetically-supramolecular' is based on the general definition of supramolecular chemistry as "…chemical systems made up of a discrete number of assembled molecular subunits or components. The forces responsible for the spatial organization may vary from weak (intermolecular forces, electrostatic or hydrogen bonding) to strong (covalent bonding), provided that the degree of electronic coupling between the molecular components remains small with respect to relevant energy parameters of the component."[52] In the present situation, 'magnetically-supramolecular' means covalently-linked magnetic molecular components (SMMs) with inter-component exchange interactions that are very weak with respect to the intra-SMM interactions.
52 https://en.wikipedia.org/w/index.php?title=Supramolecular_chemistry&oldid=679393015.
53 G. Wu, R. Clérac, W. Wernsdorfer, S. Qiu, C. E. Anson, I. J. Hewitt and A. K. Powell, *Eur. J. Inorg. Chem.*, 2006, 1927–1930.
54 V. A. Grillo, M. Knapp, J. C. Bollinger, D. N. Hendrickson and G. Christou, *Angew. Chem., Int. Ed. Engl.*, 1996, **35**, 1818–1820.
55 G. Novitchi, W. Wernsdorfer, L. F. Chibotaru, J.-P. Costes, C. E. Anson and A. K. Powell, *Angew. Chem., Int. Ed.*, 2009, **48**, 1614–1619.
56 R. Inglis, A. D. Katsenis, A. Collins, F. White, C. J. Milios, G. S. Papaefstathiou and E. K. Brechin, *CrystEngComm*, 2010, **12**, 2064–2072.
57 E. C. Sanudo, J. S. Uber, A. P. Balague, O. Roubeau and G. Aromi, *Inorg. Chem.*, 2012, **51**, 8441–8446.
58 P. Albores, C. Plenk and E. Renschler, *Inorg. Chem.*, 2012, **51**, 8373–8384.
59 H. Kumari, C. L. Dennis, A. V. Mossine, C. A. Deakyne and J. L. Atwood, *ACS Nano*, 2012, **6**, 272–275.
60 J. S. Costa, L. A. Barrios, G. A. Craig, S. J. Teat, F. Luis, O. Roubeau, M. Evangelisti, A. Camon and G. Aromi, *Chem. Commun.*, 2012, **48**, 1413–1415.
61 G. F. S. Whitehead, F. Moro, G. A. Timco, W. Wernsdorfer, S. J. Teat and R. E. P. Winpenny, *Angew. Chem., Int. Ed.*, 2013, **52**, 9932–9935.
62 J. M. Frost, S. Sanz, T. Rajeshkumar, M. B. Pitak, S. J. Coles, G. Rajaraman, W. Wernsdorfer, J. Schnack, P. J. Lusby and E. K. Brechin, *Dalton Trans.*, 2014, **43**, 10690–10694.

63 (*a*) G. F. S. Whitehead, J. Ferrando-Soria, L. G. Christie, N. F. Chilton, G. A. Timco, F. Moro and R. E. P. Winpenny, *Chem. Sci.*, 2014, **5**, 235–239; (*b*) J. Ferrando-Soria, A. Fernandez, E. M. Pineda, S. A. Varey, R. W. Adams, I. J. Vitorica-Yrezabal, F. Tuna, G. A. Timco, C. A. Muryn and R. E. P. Winpenny, *J. Am. Chem. Soc.*, 2015, **137**, 7644–7647.

64 M. Pascu, F. Lloret, N. Avarvari, M. Julve and M. Andruh, *Inorg. Chem.*, 2004, **43**, 5189–5191.

65 V. Bellini, G. Lorusso, A. Candini, W. Wernsdorfer, T. B. Faust, G. A. Timco, R. E. P. Winpenny and M. Affronte, *Phys. Rev. Lett.*, 2011, **106**, 227205.

66 A. Ardavan, A. M. Bowen, A. Fernandez, A. J. Fielding, D. Kaminski, F. Moro, C. A. Muryn, M. D. Wise, A. Ruggi, E. J. L. McInnes, K. Severin, G. A. Timco, C. R. Timmel, F. Tuna, G. F. S. Whitehead and R. E. P. Winpenny, 2015, arXiv:1510.01694.

67 (*a*) G. Aromsı, D. Aguila, P. Gamez, F. Luis and O. Roubeau, *Chem. Soc. Rev.*, 2012, **41**, 537–546; (*b*) D. Aguilà, L. A. Barrios, V. Velasco, O. Roubeau, A. Repollés, P. J. Alonso, J. Sesé, S. J. Teat, F. Luis and G. Aromí, *J. Am. Chem. Soc.*, 2014, **136**, 14215–14222.

68 K. Katoh, R. Asano, A. Miura, Y. Horii, T. Morita, B. K. Breedlove and M. Yamashita, *Dalton Trans.*, 2014, **43**, 7716–7725.

69 C. Y. Chow, H. Bolvin, V. E. Campbell, R. Guillot, J. W. Kampf, W. Wernsdorfer, F. Gendron, J. Autschbach, V. L. Pecoraro and T. Mallah, *Chem. Sci.*, 2015, **6**, 4148–4159.

70 R. Sato, K. Suzuki, M. Sugawa and N. Mizuno, *Chem.–Eur. J.*, 2013, **19**, 12982–12990.

71 K. Katoh, H. Isshiki, T. Komeda and M. Yamashita, *Coord. Chem. Rev.*, 2011, **255**, 2124–2148.

72 T. N. Nguyen, W. Wernsdorfer, K. A. Abboud and G. Christou, *J. Am. Chem. Soc.*, 2011, **133**, 20688–20691.

73 J. B. Vincent, H. R. Chang, K. Folting, J. C. Huffman, G. Christou and D. N. J. Hendrickson, *J. Am. Chem. Soc.*, 1987, **109**, 5703–5711.

74 Although almost all lattice CH_2Cl_2 molecules are disordered, the two encapsulated ones are ordered and were included in the refinement cycles.

75 *SHELXTL6*, Bruker-AXS, Madison, Wisconsin, USA, 2008.

76 See ESI†

77 (*a*) E. R. Davidson, *MAGNET*, Indiana University: Bloomington, IN, 1999; (*b*) E. R. Davidson, *GRID*, Indiana University: Bloomington, IN, 2000.

78 W. Wernsdorfer, *Adv. Chem. Phys.*, 2001, **118**, 99–190.

79 A. K. Hassan, L. A. Pardi, J. Krzystek, A. Sienkiewicz, P. Goy, M. Rohrer and L. C. Brunel, *J. Magn. Reson.*, 2000, **142**, 300–312.

80 T. C. Stamatatos, D. Foguet-Albiol, S.-C. Lee, C. C. Stoumpos, C. P. Raptopoulou, A. Terzis, W. Wernsdorfer, S. Hill, S. P. Perlepes and G. Christou, *J. Am. Chem. Soc.*, 2007, **129**, 9484–9499.

81 C. Papatriantafyllopoulou, G. Aromi, A. J. Tasiopoulos, V. Nastopoulos, C. P. Raptopoulou, S. J. Teat, A. Escuer and S. P. Perlepes, *Eur. J. Inorg. Chem.*, 2007, 2761–2774.

82 P. Chaudhuri, T. Weyhermuller, R. Wagner, S. Khanra, B. Biswas, E. Bothe and E. Bill, *Inorg. Chem*, 2007, **46**, 9003–9016.

83 C. C. Stoumpos, T. C. Stamatatos, H. Sartzi, O. Roubeau, A. J. Tasiopoulos, V. Nastopoulos, S. J. Teat, G. Christou and S. P. Perlepes, *Dalton Trans.*, 2009, 1004–1015.

84 C. Lampropoulos, T. C. Stamatatos, M. J. Manos, A. J. Tasiopoulos, K. A. Abboud and G. Christou, *Eur. J. Inorg. Chem.*, 2010, 2244–2253.

85 C. D. Polyzou, H. Nikolaou, C. Papatriantafyllopoulou, V. Psycharis, A. Terzis, C. P. Raptopoulou, A. Escuer and S. P. Perlepes, *Dalton Trans.*, 2012, **41**, 13755–13764.

86 D. Dermitzaki, C. P. Raptopoulou, V. Psycharis, A. Escuer, S. P. Perlepes and T. C. Stamatatos, *Dalton Trans.*, 2014, **43**, 14520–14524.

87 A. Chakravorty, *Coord. Chem. Rev.*, 1974, **13**, 1–46.

88 P. Chaudhuri, *Coord. Chem. Rev.*, 2003, **243**, 143–190.

89 C. J. Milios, T. C. Stamatatos and S. P. Perlepes, *Polyhedron*, 2006, **25**, 134–194.

90 E. C. Constable, J. Lewis, M. C. Liptrot and P. R. Raithby, *Inorg. Chim. Acta*, 1990, **178**, 47–54.

91 M. W. Wemple, H.-L. Tsai, K. Folting, D. N. Hendrickson and G. Christou, *Inorg. Chem.*, 1993, **32**, 2025–2031.

92 H. J. Eppley, H.-L. Tsai, N. de Vries, K. Folting, G. Christou and D. N. Hendrickson, *J. Am. Chem. Soc.*, 1995, **117**, 301–317.

93 Z. Sun, D. Ruiz, N. R. Dilley, M. Soler, J. Ribas, K. Folting, M. B. Maple, G. Christou and D. N. Hendrickson, *Chem. Commun.*, 1999, 1973–1974.

94 M. Soler, S. K. Chandra, D. Ruiz, E. R. Davidson, D. N. Hendrickson and G. Christou, *Chem. Commun.*, 2000, 2417–2418.

95 B. Fleury, L. Catala, V. Huc, C. David, W. Z. Zhong, P. Jegou, L. Baraton, S. Palacin, P.-A. Albouyd and T. Mallah, *Chem. Commun.*, 2005, 2020–2022.

96 J. J. Henderson, C. M. Ramsey, E. D. Barco, A. Mishra and G. Christou, *J. Appl. Phys.*, 2007, **101**, 09E102.

97 A. M. Mowson, T. N. Nguyen, K. A. Abboud and G. Christou, *Inorg. Chem.*, 2013, **52**, 12320–12322.

98 K. J. Kambe, *J. Phys. Soc. Jpn.*, 1950, **5**, 48–51.

99 J. H. Van Vleck, *The Theory of Electric and Magnetic Susceptibilities*, Oxford University Press, 1932.

100 J. Cano, T. Cauchy, E. Ruiz, C. J. Milios, C. C. Stoumpos, T. C. Stamatatos, S. P. Perlepes, G. Christou and E. K. Brechin, *Dalton Trans.*, 2008, 234–240.

101 M. Atanasov, B. Delley, F. Neese, P. L. Tregenna-Piggott and M. Sigrist, *Inorg. Chem.*, 2011, **50**, 2112–2124.

102 C. Lampropoulos, K. A. Abboud, T. C. Stamatatos and G. Christou, *Inorg. Chem.*, 2009, **48**, 813–815.

103 N. Aliaga-Alcade, R. S. Edwards, S. Hill, W. Wernsdorfer, K. Folting and G. Christou, *J. Am. Chem. Soc.*, 2004, **126**, 12503–12516.

104 J. Yoo, A. Yamaguchi, M. Nakano, J. Krzystek, W. E. Streib, L.-C. Brunel, H. Ishimoto, G. Christou and D. N. Hendrickson, *Inorg. Chem.*, 2001, **40**, 4604–4616.

105 S.-I. Chen, C. C. Beedle, P.-R. Gan, G.-H. Lee, S. Hill and E.-C. Yang, *Inorg. Chem.*, 2012, **51**, 4448–4457.

106 S. Hill, R. S. Edwards, S. I. Jones, N. S. Dalal and J. M. North, *Phys. Rev. Lett.*, 2003, **90**, 217204.
107 S. Takahashi, R. S. Edwards, J. M. North, S. Hill and N. S. Dalal, *Phys. Rev. B: Condens. Matter Mater. Phys.*, 2004, **70**, 094429.
108 S. Stoll and A. Schweiger, *J. Magn. Reson.*, 2006, **178**, 42–55.
109 L. Landau, *Phys. Z. Sowjetunion*, 1932, **2**, 46–51.
110 C. Zener, *Proc. R. Soc. London, Ser. A*, 1932, **137**, 696–702.